

TUNABLE SECOND HARMONIC GENERATION DEVICES  
WITH AN INTEGRATED MICRO-HEATER

TUNABLE SECOND HARMONIC GENERATION DEVICES  
WITH AN INTEGRATED MICRO-HEATER

By

YI GAN, B. Sc.

A Thesis

Submitted to the School of Graduate Studies

in Partial Fulfillment of the Requirements

for the Degree

Master of Applied Science

McMaster University

© Copyright by Yi Gan, October 2008

MASTER OF APPLIED SCIENCE (2008)  
(Engineering Physics)

McMaster University  
Hamilton, Ontario

TITLE: Tunable Second Harmonic Generation Devices  
with an Integrated Micro-heater

AUTHOR: Yi Gan, B. Sc.  
(Huazhong University of Science and Technology)

SUPERVISOR: Professor Chang-Qing Xu

NUMBER OF PAGES: X, 102

## **Abstract**

Single-pass frequency conversion by a nonlinear optical crystal is an attractive method to generate coherent radiation in various spectral domains from ultraviolet to mid-infrared. Wavelength converters based on quasi-phase matched (QPM) periodically poled lithium niobate (PPLN) have proved to be important wavelength conversion devices for many useful applications. This thesis develops a novel integration design for temperature controlling and temperature wavelength tuning of a QPM-PPLN waveguide wavelength converter. A Cr/Pt/Au thin film alloy layer is deposited on a PPLN device with a polymer buffer layer to work as a micro-heater and a temperature sensor at the same time. The temperature of the device can be tailored by applying current to the micro-heater layer, which changes the effective period of the QPM grating and thus the QPM wavelength through the thermal optical effect (TOE). The device's temperature can be monitored by measuring the resistance change of the alloy layer. Micro-heater design and mode profile simulation are involved in the thesis. The entire device fabrication process is introduced. Both electrical and optical features of the device are characterized and discussed. In contrast to the conventional temperature tuning method based on a bulky oven, the proposed design has some excellent characteristics such as compact package size and low power consumption.

## Acknowledgements

First, I would like to thank my supervisor, Dr. Chang-Qing Xu, who has offered me enormous support, great encouragement and expert guidance in various aspects throughout my M. A. Sc. Program. His patience, enthusiasm and dedication made my past two years time in McMaster University a truly positive and enriching experience.

Thanks to Dr. Wan-Guo Liang for all the help in device fabrication and characterization. This work would not have been finished without his great efforts. Working with Dr. Liang has been a wonderful experience for me. Thanks to Dr. Toshiaki Suhara and Dr. Masatoshi Fujimura from Osaka University in Japan for their constant encouraging and enlightening suggestions when I attended the AMP2008 program in July 2008. Thanks to Dr Xijia Gu from Ryerson University for his remarkable help on fiber lasers and FBG research work.

Thanks to Dr. Paul Jessop and Dr. Ray LaPierre for their two important courses on optoelectronics and thin film technologies. Thanks all the professors in the Department of Engineering Physics for their valuable suggestions on my research work. Thanks Doris V. Stevanovic and Zhilin Peng from CEDT for their training courses about clean room

and assistance in the clean room. Thanks also to Fran, Marilyn, Linda and Lori for all their help in the Engineering Physics office.

Thanks Fangfang Zhang for the help to set up experiments in the lab and teach me the characterization skills. Thanks to Dr. Jian Yang and Qiang-yang Xu for their invaluable advice and discussions on my research topics. Thanks also to Andrea Greening to help me checking my English writing. I am also appreciative to my colleagues, Juan Deng, Ling Han, and Pawan Sandhu. It's been great getting to know you, to learn from you and to work with you.

Last but not least, I would like to thank my parents and other family members for their lifelong encouragement and support.

# Table of Contents

## CHAPTER 1

<b>INTRODUCTION .....</b>	<b>1</b>
1.1 Overview of Wavelength Conversions.....	1
1.2 General Applications of Wavelength Converters .....	6
1.3 Motivation of the Research.....	13
1.4 Thesis Outline .....	16

## CHAPTER 2

<b>FUNDAMENTALS OF LITHIUM NIOBATE QUASI-PHASE-MATCHED WAVELENGTH CONVERTERS .....</b>	<b>18</b>
2.1 Nonlinear Optical Interactions .....	18
2.2 Wave Equation and Coupled-Mode equation .....	22
2.3 Phase Matching.....	29
2.4 Properties of Lithium Niobate .....	35
2.5 Temperature Dependence of QPM-LiNbO <sub>3</sub> .....	40

## CHAPTER 3

<b>MICRO-HEATER DESIGN AND WAVEGUIDE MODE PROFILE .....</b>	<b>44</b>
3.1 Micro-Heater Design.....	44
3.2 Waveguide Mode profile.....	54

## CHAPTER 4

<b>DEVICE FABRICATION .....</b>	<b>60</b>
4.1 Fabrication of QPM Gratings .....	61
4.2 Fabrication of Waveguides .....	64
4.3 Buffer Layer, Micro-heater and Dicing .....	68

**CHAPTER 5**

**EXPERIMENTS AND RESULTS DISCUSSION ..... 71**

- 5.1 Wavelength Converter Packaging ..... 71
- 5.2 Electrical characterization..... 79
- 5.3 Optical characterization ..... 84

**CHAPTER 6**

**CONCLUSION ..... 92**

- 6.1 Summary of Research Achievements ..... 92
- 6.2 Suggestions for Future Work..... 93

**BIBLIOGRAPHY ..... 94**

## List of Figures

Figure 1.1 Characteristics of wavelength conversion types .....	2
Figure 2.1 Electric polarization in a dielectric material .....	18
Figure 2.2 Geometry of two wave interaction .....	20
Figure 2.3 Energy-level diagram describing SHG .....	22
Figure 2.4 Dependence of SHG efficiency on interaction length under power depletion assumption and power nondepletion assumption .....	28
Figure 2.5 Effects of phase mismatch on the SHG conversion efficiency .....	29
Figure 2.6 Growth of SHG power along the propagation direction with different phase mismatch.....	30
Figure 2.7 Growth of second-harmonic power in a nonlinear crystal with phase matching (dashed curve), without phase matching (dotted curve), and with quasi-phase matching (solid curve).....	33
Figure 2.8 Lithium Niobate Crystal .....	36
Figure 2.9 Hexagonal crystal structure of $\text{LiNbO}_3$ .....	38
Figure 2.10 (a) para-electric phase of $\text{LiNbO}_3$ (b) ferro-electric phase of $\text{LiNbO}_3$ .....	39
Figure 2.11 Temperature dependence of the QPM period (a) and wavelength (b) .....	42
Figure 3.1 Device structure diagram .....	46
Figure 3.2 Straight line micro-heater .....	48
Figure 3.3 SHG tuning curve without current injection (a) and with current injection (b).....	49
Figure 3.4 Square wave micro-heater .....	49
Figure 3.5 Dimension and top view of micro heater area.....	50
Figure 3.6 Lumped Parameter Thermal Model for integration structure .....	51
Figure 3.7 Diagram of effective conductivity calculation .....	52
Figure 3.8 Temperature change versus current injection .....	53
Figure 3.9 Current dependence of QPM wavelength change .....	53
Figure 3.10 Refractive index distributions in PE (a) and APE (b) waveguide .....	56
Figure 3.11 Fundamental TM mode profile for APE $\text{LiNbO}_3$ waveguide (a) and APE $\text{LiNbO}_3$ waveguide with a polymer buffer layer (b) .....	59

Figure 4.1 Fabrication Process for PPLN with integrated micro-heater .....	60
Figure 4.2 Liquid electrode poling setup .....	62
Figure 4.3 Microscopic picture of PPLN surface .....	63
Figure 4.4 Equipment setup for proton-exchange .....	65
Figure 4.5 Equipment setup for annealing .....	66
Figure 4.6 Comparisons of APE and RPE waveguides .....	67
Figure 4.7 Equipment setup for RPE process .....	68
Figure 4.8 Lift-off process .....	69
Figure 4.9 A microscopic picture of the micro-heater .....	70
Figure 5.1 A transverse misalignment between a fiber and a waveguide .....	72
Figure 5.2 A longitudinal misalignment between a fiber and a waveguide .....	72
Figure 5.3 An angular misalignment between a fiber and a waveguide .....	73
Figure 5.4 The fiber-to-waveguide connected by UV curable epoxy .....	75
Figure 5.5 A UV epoxy fiber-waveguide connection joint .....	77
Figure 5.6 Experimental setup for the fiber-waveguide connection package .....	78
Figure 5.7 Output Power dependence upon Temperature .....	78
Figure 5.8 Electrical characterization setup .....	80
Figure 5.9 Micro-heater Resistance versus Temperature .....	81
Figure 5.10 Temperature change with 25 mA injection current .....	82
Figure 5.11 Temperature change with 125 mA injection current .....	83
Figure 5.12 A schematic diagram of temperature tuning process .....	84
Figure 5.13 Experimental setup for wavelength tuning range test .....	85
Figure 5.14 Broadband source + EDFA output spectrum .....	86
Figure 5.15 Alignment apparatus of the QPM-PPLN with integrated micro heater .....	87
Figure 5.16 Additional equipments used for test .....	87
Figure 5.17 Theoretical and experimental SHG tuning curve .....	88

Figure 5.18 SHG output spectrums under different injection currents .....	90
Figure 5.19 QPM wavelength versus injection current .....	90

### List of Tables

Table 1.1 Comparison of Wavelength conversion techniques .....	3
Table 2.1 Comparison of QPM and BPM .....	34
Table 2.2 Basic properties of lithium niobate crystal .....	36
Table 2.3 Parameters of Sellmeier equation .....	41

## CHAPTER 1

### INTRODUCTION

#### 1.1 Overview of Wavelength Conversions

Since the invention of the first laser in the 1960s, the wavelength conversion of laser radiation has become an important technique widely used for solving various scientific and engineering problems. Especially in the past few decades, wavelength conversion technology has attracted more and more attention because of the increased requirement from the optical communications industry [1] and solid state laser field [2].

The fundamental physics of wavelength conversion is now reasonably well understood. In some nonlinear materials, given sufficient optical input power, electric dipoles of the new harmonic different than the incident wave can be generated. These new dipoles generate light at different frequencies that can be used independently, or to create new optical waves at other frequencies when interacting with input waves. The wavelength conversion devices must be fabricated with a technique called phase matching, which compensates the difference in phase velocity between the fundamental wave and its harmonic in a nonlinear material caused by natural dispersion. This technique ensures that the electric field

amplitudes of all the newly generated waves in the material add constructively to achieve maximum output power.

Wavelength converters may be fabricated on a variety of materials, including semiconductors [3], nonlinear optical crystals [4], optical fibers [5] and organic polymers [6]. A material with a high nonlinear coefficient is required to achieve high conversion efficiency. Different materials are best suited for different wavelength conversion techniques. In general, wavelength conversion techniques can be categorized into three types: optoelectronic (OE-EO), optical switching and optical mixing [1]. The latter two are all-optical types. Table 1.1 and Fig 1.1 show the comparisons of various wavelength conversion techniques.

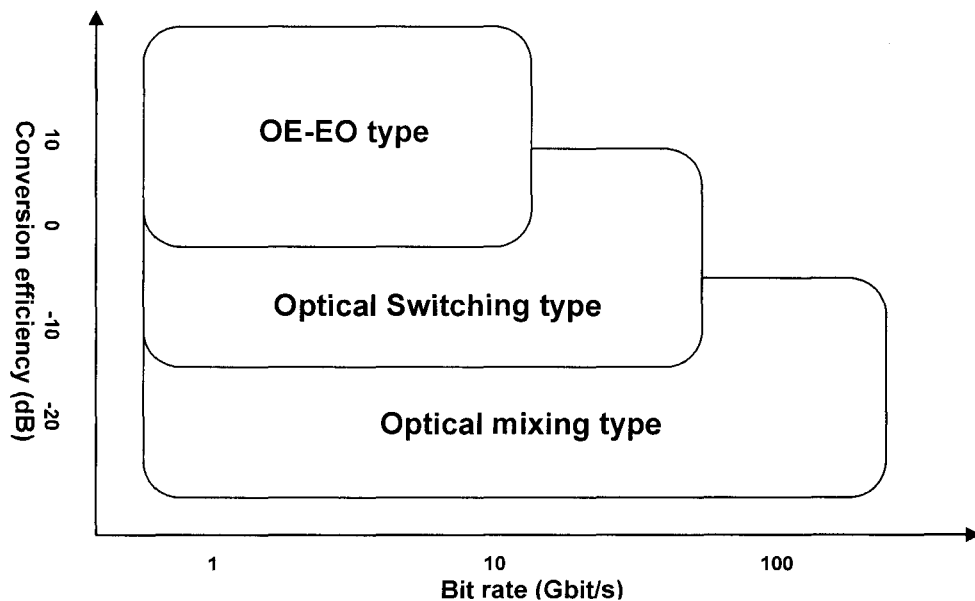


Figure 1.1 Characteristics of wavelength conversion types [1]

	OE/EO	All-optical conversion				
		Optical Switching Type			Optical Mixing Type	
		XGM	XPM	DPM	DFG	FWM
Typical Device	PD/LD/IC	SOA LD	SOA MZ	SOA MZ	QPM PPLN	SOA Fiber
Data rate	~40 Gbit/s	~40 Gbit/s	~40 Gbit/s	~160 Gbit/s	~1 Tbit/s	~1 Tbit/s
Transparency	None/digital	Digital	Digital	Digital	Strict	Strict
Conversion efficiency	Excellent	Good	Good	Good	Fair	Fair
Polarization insensitivity	Yes	Yes	Yes	Yes	No	No
Bandwidth	Depends on light source	~30 nm	~30 nm	~30 nm	~60 nm	~40 nm
Chirp	Small	High	Small	Small	Reverse	Reverse
Advantages	Ready for deployment, regeneration of the signal	Simple configuration	Reduced chirp, distortion	Higher data rate	Transparency, broad bandwidth	Transparency
Disadvantages	Limited bandwidth and cost	High noise, signal degradation and chirp	Narrow input dynamic range	Narrow input dynamic range	Low conversion efficiency, polarization dependent	Low conversion efficiency and bandwidth, large spontaneous noise, polarization dependent

Table 1.1 Comparison of Wavelength conversion techniques [1, 7]

Optoelectronic wavelength conversion is the most straightforward conversion technique. In this type, the input optical signal is converted to the electronic signal by a photo detector. Then after electronic amplification, reshaping and re-timing, the electronic signal is converted back to an optical signal by a laser at a different wavelength.

Optoelectronic conversion is a more readily applicable compared to others due to the mature and low cost optoelectronic devices, such as distributed feedback (DFB) lasers, semiconductor photo detectors and integrated circuits. The limitation of optoelectronic wavelength conversion is the poor transparency of the signal format and bit rate, which have become a bottleneck in high speed optical fiber communication systems.

In all-optical wavelength conversion, optical signals are directly converted to different wavelength signals without going through OE or EO devices. Using all-optical conversion techniques greatly enhances the conversion speed and has excellent transparency to signal format, which is very important for photonic networks.

While the optoelectronic technique will still remain in the market, several all-optical techniques have been demonstrated to implement wavelength conversion. These can be either incoherent techniques (optical switching) or coherent techniques (optical mixing).

The principle of optical switching type wavelength conversion is that a signal light drives an optical switch to convert the signal light to a

different wavelength signal light and the bit patterns of the input are copied to the output [7]. This type wavelength converter is usually based on semiconductor materials. It includes cross-gain modulation (XGM), cross phase modulation (XPM) and differential phase modulation (DPM). The XGM type is based on carrier density variation in a semiconductor optical amplifier (SOA) caused by the input signal light. The XPM and DPM types are based on an interference switch that uses refractive index change in the SOAs caused by the input signal light. The merits of these optical switching type converters include simplicity, polarization independency, good power efficiency and reasonably high bit rate. On the other hand, the shortcomings are obvious. The SOA converters will add spontaneous emission noise to the converted signals, the carrier life time limits the bit rate (XGM, XPM) and the operation stability is still a problem (DPM).

Optical mixing type wavelength converters are based on the nonlinear optical response of a material. The signal light and a pump light interact with each other and generate a third wavelength due to the second-order (DFG) or third-order (FWM) nonlinear susceptibility of the medium [8, 9]. The phase and amplitude information of the signal light is completely transferred to the third light, which means the optical mixing type wavelength converters are strictly transparent to the signal format. Moreover, it achieves wavelength conversion with wide wavelength bandwidth at very high bit rate. Since there is no active device involved,

the nonlinear parametric process is usually free of excess noise. However, optical mixing type wavelength conversion is polarization dependent and needs some phase matching techniques to compensate the difference in phase velocity, especially for the second order nonlinear process.

Among the large number of nonlinear materials that can be used for wavelength conversion, lithium niobate ( $\text{LiNbO}_3$ ) crystals have proven to be one of the most attractive choices. Especially since researchers have developed the mature and commercial techniques to achieve quasi-phase matching in lithium niobate crystal, which could dramatically enhance the second order nonlinear efficiency. Currently, QPM- $\text{LiNbO}_3$  wavelength conversion devices have been widely researched for the entire transparency window of lithium niobate.

## **1.2 General Applications of Wavelength Converters**

Wavelength converters offer a variety of important applications in the photonics field. These applications include optical data storage [2], spectroscopy [10], optical gating and switching [11], UV and visible light generation [2], optical sampling [12], soliton formation [13], and environmental monitoring [14]. The emerging demands from the optical communications field and solid state lasers field have recently accelerated the development of wavelength converters.

***WDM optical communications network***

This is an exciting time for telecommunications. The use of the Internet has completely changed people's lives. Consequently, the dramatic increase of data transmission has also brought a huge change to the telecommunications network all over the world. The increasing amount of communication traffic means that more and more capacity is required for the network system. For this purpose, wavelength division multiplexing (WDM) technologies have been developed to replace the time division multiplexing (TDM) technique to enhance the capacity of optical networks. In WDM systems, multiple independent signal channels carried by different wavelengths are simultaneously transmitted through the same fiber, which upgrades the capacity and flexibility of communication networks to a whole new level.

Currently, wavelength conversion devices have been recognized as one of the key devices for the WDM network because they decrease the channel blocking probability and make it possible to reuse wavelengths at each cross-connect node [15]. The efficient use of wavelength resources can furthermore increase the flexibility of the network. To meet the requirements for WDM networks, a wavelength conversion device has to have highly efficient conversion, high bit rate, low noise, transparency to optical signal formats, and polarization insensitivity. Wavelength converters should also be cascadable, have a

wide input power dynamic range, and operate using the same wavelength as the input one.

In WDM networks, although OE-EO type wavelength converters are still the mainstream in the market, all-optical wavelength converters are expected to dominate the future. Both optical switching type and optical mixing type wavelength conversion devices have been proposed and studied in some experimental WDM networks systems, but quasi-phase-matched LiNbO<sub>3</sub> (QPM-LN) waveguides are superior to the others. They can convert high-speed signals of 1 THz or more, have no signal-to-noise ratio (SNR) degradation and no signal format dependence, and can simultaneously convert a group of broadband wavelengths [3]. QPM LiNbO<sub>3</sub> waveguides are conventionally fabricated by the annealed proton exchange (APE) technique [16]. The commonly used techniques are the DFG and cascaded second harmonic generation (SHG) and DFG. In order to eliminate the wavelength shift caused by photorefractive damage, the devices normally need to be heated over 100 °C or use MgO- or ZnO doped LiNbO<sub>3</sub> which are more damage resistant [17].

### ***Laser sources***

Since T. Maiman demonstrated the first working laser in 1960, lasers have become one of the most important tools not only in scientific research fields but also in people's everyday life. Historically, laser applications have been limited by the restricted number of laser

wavelengths or colours that are conveniently available. The two largest laser applications are optical storage devices, such as CDs and DVDs, and fiber optical communication. These two fields have both benefited from the great research achievements of visible and near-infrared semiconductor lasers. However, the semiconductor lasers operating at wavelengths in ultraviolet, blue-green-yellow and longer than  $2\ \mu\text{m}$  are still not commercialized. There are many promising laser applications in these ranges have not seen commercial deployment, such as dense optical data storage, bio-research, color display and environmental monitoring [2]. Currently, the gas or dye lasers and some quantum cascaded lasers available in these ranges are still relatively bulky, fragile and expensive. Moreover, most of them have a short lifetime and require professional maintenance or special working conditions. A series of compact lasers cover these regions would be more desirable.

Only one year after the invention of the laser, Franken's initial second harmonic generation experiment opened a new way to achieve the laser at certain wavelengths [18]. Combining nonlinear crystals and currently commercial semiconductor lasers or solid-state lasers, a highly efficient laser output in the wavelength range from UV to Mid-IR can be achieved by some wavelength conversion techniques.

The short wavelength of UV lasers makes them particularly desirable for many industrial applications. Light in the UV range permits

various types of non-thermal (cold) processing. These applications include the removal of sub-micrometer-thick layers of material as in laser eye surgery, marking an object by UV photon induced color changes of the surface, and UV lithography for fabricating nano scale structured devices [19]. Historically, most ultraviolet (UV) applications relied primarily on UV lamps. In the past decades, the development of the excimer and solid-state UV lasers gave researchers access to higher-power UV radiation. QPM-SHG wavelength conversion is one of the most attractive methods for generating a UV light source with compact size systems because it has significant advantages in phase matching arbitrary wavelengths and in reaching high nonlinear coefficients by using of an appropriate period of domain inversion. Generation of UV light by QPM-SHG has been reported for bulk- and waveguide-type devices made from  $\text{LiNbO}_3$ ,  $\text{LiTaO}_3$ , and  $\text{KTiOPO}_4$  [20, 21]. However, generation of UV light from QPM materials has several limitations, such as low transparency at UV wavelengths, difficulties in fabricating a first-order nonlinear grating, and optical damage. These limitations can be overcome by using periodically poled magnesium oxide (MgO) doped or stoichiometric  $\text{LiNbO}_3$ . Moreover, MgO doped  $\text{LiNbO}_3$  has shorter cut-off wavelength, which extends to 320 nm, and higher resistance to photorefractive damage [22]. Periodically poled MgO doped  $\text{LiNbO}_3$  is thus attractive for the generation of radiation in the UV even below 355 nm. At this time, researchers are still trying to develop

suitable poling techniques to produce a period of less than  $2\ \mu\text{m}$  in a Z-cut crystal for the first-order QPM-UV-SHG.

Recently, compact reliable visible lasers have attracted a great amount of research attention since the laser-based display technology is expected to be a superior alternative to existing display systems in large screen projection market for business and home theatre [23]. Laser light sources can provide extremely wide color expression with faster response time and longer life time than any lamp light sources. For the three additive primary colors, red, green, and blue (RGB), the red semiconductor laser diodes are already commercially available. Several companies have developed blue laser diodes with output power in the order of Watts, but their cost and life time are still need more improvements [24]. Reportedly, semiconductor laser diodes in the green region will not be available for many years at power levels and at wavelengths suitable for display applications. Traditional gas- and dye-based green lasers emitting blue-green light are limited by their large size, inefficient, and cumbersome maintainance. Therefore, combining solid state lasers and appropriate wavelength conversion techniques seems to be the only alternative to achieve highly efficient and economical multi-watt blue-green lasers at this time. Research groups around the world have already achieved visible lasers by wavelength conversion techniques with several watts or even tens of watts of output power for CW and

thousands of watts of peak power for pulsed lasers. Besides display applications, these blue-green lasers can also be used for dense optical data storage, biotechnologies, and submarine communications [2].

There are many military and commercial applications for the laser in the Mid-infrared (Mid-IR) region, which is located in the spectroscopy from about 2  $\mu\text{m}$  to 5  $\mu\text{m}$ . These applications, such as environmental monitoring (chemical sensors and gas detection), biomedical analysis, and high-resolution spectroscopy, attract many research groups all over the world to develop high power, compact and low cost Mid-IR laser sources. Various methods have been proposed and studied to generate a Mid-IR laser, such as antimonide diode lasers [25], quantum cascade technology [26], lead-salt tunable diode lasers[27], tunable solid-state lasers and wavelength conversion techniques [14, 28]. Among the reported mid-IR light generation techniques, those based on DFG in a periodically poled nonlinear medium or other nonlinear optical crystals have attracted special attention due to broad tunable wavelength region, narrow linewidth, room temperature operation, low noise, low power consumption, compact size and ruggedness. The drawback of this method is that it is difficult to couple the lights into the crystal since the wavelength difference is large in the DFG process and the output power generated from this process is lower. Recently, NTT developed a ridge waveguide device based on PPLN to overcome this problem. The ridge structure confines both the

input and output light in a waveguide with a less than  $100 \mu\text{m}^2$  cross-section area, which has greatly increased the conversion efficiency [29, 30].

### **1.3 Motivation of the Research**

Two different designs have been used to achieve SHG conversion: intra-cavity and single-pass. While intra-cavity designs tend to achieve higher efficiencies than single-pass structures, they are significantly harder to construct and take a long time to implement. Highly efficient single-pass SHG is therefore desirable for generating coherent radiation in various spectral domains from ultraviolet to mid-infrared. Over the years,  $\text{LiNbO}_3$  has been the most attractive material of choice for frequency conversion, because it is a mature and readily available material with a large second-order nonlinear coefficient and wide transparency bandwidth covering a useful range from 350 to 5000 nm. To achieve efficient frequency conversion, a phase matching technique has to be employed to compensate the phase matching between the interacting waves. Recently, the QPM technique has been recognized as an attractive method to achieve efficient wavelength conversion. Compared with other phase matching methods such as birefringent phase matching (BPM) technique, the QPM technique allows the use of the largest nonlinear coefficient over

the whole transparent spectral range of the crystal without the walk-off effect.

The QPM condition is closely related to the periodic structure along the propagation direction, so the tolerance of QPM devices to temperature variations and wavelength are usually small. In other words, the operation temperature and the fundamental wavelength have to be controlled in a narrow region to satisfy the QPM condition. As a result, a temperature control system is usually required for the QPM devices to achieve stable operation. Moreover, the PPLN devices normally need to be heated over 100 °C to eliminate the refractive index change caused by photorefractive damage. Even devices based on more damage resistant MgO- or ZnO-doped LiNbO<sub>3</sub>, are usually operated at a temperature higher than room temperature (about 60 °C) to remove any possible effects of the photorefractive damage [17].

On the other hand, in some biomedical or environmental monitoring applications, it is desirable to tune the converted wavelength. Several methods have been studied to achieve tunable QPM devices, such as angle tuning [31], aperiodic QPM grating [32, 33], tapered waveguide [34] and temperature tuning [35]. Compared with other tuning methods, temperature tuning is more attractive because of its simplicity. When the temperature is tuned, the QPM period is effectively changed due to the temperature dependence of the refractive indexes. Moreover, the

temperature tuning technique can maintain the conversion efficiency over in the entire tuning range, which can barely be achieved by the other tuning techniques.

Conventional temperature controlling and tuning methods often include external oven (for bulk devices) or TEC (for waveguide devices), which are usually cost high power consumption and cannot achieve fast tuning. In many PPLN experiments, an external oven from Thorlabs (model PV40) is used to heat the devices. The volume of the oven is about  $60 \text{ cm}^3$ . Additionally, it requires a heater controller (Thorlab, model TC200) to supply the power and control the temperature. The heater controller can control the oven's temperature from room temperature to  $200 \text{ }^\circ\text{C}$  with a resolution of  $0.1 \text{ }^\circ\text{C}$ . The power consumption of this heating system is  $25 \text{ W}$ . In commercial PPLN packages, semiconductor thermal electric coolers (TEC) are used for temperature controlling. The volume of TECs is usually about several cubic centimetres, and the power consumption is several Watts or tens of Watts. In this project, we demonstrate a novel design which integrates a micro heater structure with a conventional PPLN wavelength converter to achieve compact, low power consumption temperature controlling and fast tuning method. A Cr/Pt/Au multilayer metal thin film is deposited on a PPLN sample with a polymer buffer layer to work as a micro-heater. When applying current to the micro-heater, the temperature in the micro-heater area is tuned.

Therefore, the effective period of the QPM waveguide device is changed due to the temperature dependence of the refractive index of PPLN, which ultimately leads to the change of QPM wavelength.

## **1.4 Thesis Outline**

This thesis contains a total of 6 chapters. The primary goal of this thesis is to demonstrate a novel compact integration design for tunable lithium niobate wavelength converters.

Chapter 2 provides a general introduction to the fundamentals of lithium niobate wavelength converters. It includes the nonlinear mechanisms behind the wavelength conversion process and a description of properties of lithium niobate crystal. Since we use a temperature tuning method, the temperature dependence of lithium niobate devices is also discussed.

Chapter 3 places emphasis on device design. The design of micro-heater structure is briefly introduced at first. Then there is some discussion about the change of the mode profile of the annealed proton exchanged (APE) waveguide after it has been covered by a polymer layer.

Chapter 4 introduces the whole fabrication process, from QPM grating fabrication, APE waveguide, and micro-heater deposition.

Chapter 5 describes the experiment setups and the discussion about all the experiment results. In order to avoid the misalignment caused by the different thermal expansion of lithium niobate and fiber, some basic packaging experiments are applied first. Then, both electrical and optical features of the device have been examined.

Chapter 6 concludes with a summary of the most important achievements in this thesis and suggestions for future work.

## CHAPTER 2

# FUNDAMENTALS OF LITHIUM NIOBATE QUASI-PHASE-MATCHED WAVELENGTH CONVERTERS

### 2.1 Nonlinear Optical Interactions

Optical mixing type wavelength conversion is based on the nonlinear optical properties of certain dielectric materials. A dielectric material is made up of atoms comprising a positively charged nucleus surrounded by an electron cloud (Figure 2.1). In equilibrium conditions, the positive and negative charges form a symmetrical structure. When an external electric field is applied on the material, the electric force distorts the electron cloud. This distortion causes a separation of the centers of positive and negative charges. The displacement of negative charge center from positive charge center is called polarization [2].

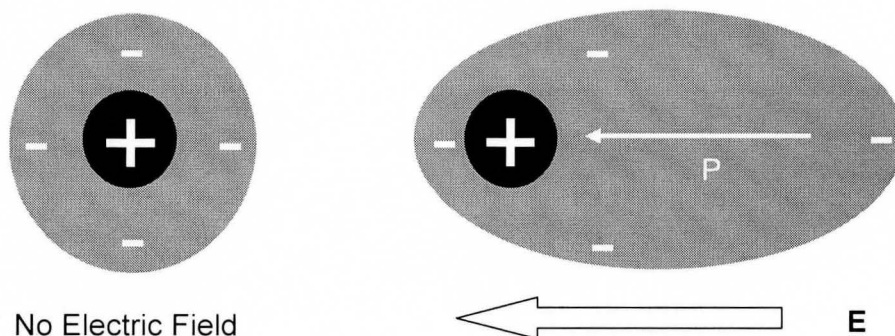


Figure 2.1 Electric polarization in a dielectric material

All dielectric materials have a macroscopic electric polarization density ( $\mathbf{P}$ ) which can be mathematically described as a power series of the applied electric field ( $\mathbf{E}$ ):

$$\mathbf{P} = \varepsilon_0\chi^{(1)}\mathbf{E} + \varepsilon_0\chi^{(2)}\mathbf{E}^2 + \varepsilon_0\chi^{(3)}\mathbf{E}^3 + \dots \quad (2.1)$$

where  $\varepsilon_0$  is the dielectric permittivity of the vacuum,  $\chi$  is known as the dielectric susceptibility.  $\chi^{(1)}$  and  $\chi^{(n)}$  is the linear and n-th order nonlinear susceptibility, respectively. In the case of conventional linear optics, since  $\chi^{(1)} \gg \chi^{(2)}$ , and the applied electric field strength is not that strong, the high order part can be ignored. The induced polarization depends linearly upon the electric field strength:

$$\mathbf{P} = \varepsilon_0\chi^{(1)}\mathbf{E} \quad (2.2)$$

this first term does not produce new frequency components, and is only responsible for the linear optical phenomena such as refraction, diffraction, and dispersion.

When studying the interaction between a laser beam and a certain medium, the electric field strength is so strong that the high order terms cannot be ignored. For most materials,  $\chi^{(2)} \gg \chi^{(3)}$ , so the second order nonlinear phenomenon is easy to observe in these materials when interacting with lasers. The second order term in equation (2.1):

$$\mathbf{P}^{(2)} = \varepsilon_0\chi^{(2)}\mathbf{E}^2 \quad (2.3)$$

is so called second order nonlinear polarization. Generally, three-wave mixing takes place through the second-order nonlinear polarization.

The nonlinear polarization acts as the source of new frequency components of the electromagnetic field. If we consider two light fields with two different frequencies,  $\omega_1$  and  $\omega_2$ , impinging on the crystal:

$$\mathbf{E} = \mathbf{E}_1 \cos(\omega_1 t) + \mathbf{E}_2 \cos(\omega_2 t) \quad (2.4)$$

then the second order nonlinear polarization then becomes:

$$\begin{aligned} \mathbf{P}_2 &= \varepsilon_0 \chi^{(2)} [\mathbf{E}_1^2 \cos^2(\omega_1 t) + \mathbf{E}_2^2 \cos^2(\omega_2 t) + \mathbf{E}_1 \mathbf{E}_2 \cos(\omega_1 t) \cos(\omega_2 t)] \\ &= \varepsilon_0 \chi^{(2)} \left[ \frac{1}{2} (\mathbf{E}_1^2 + \mathbf{E}_2^2) + \frac{1}{2} \mathbf{E}_1^2 \cos(2\omega_1 t) + \frac{1}{2} \mathbf{E}_2^2 \cos(2\omega_2 t) \right. \\ &\quad \left. + \varepsilon_0 \chi^{(2)} [\mathbf{E}_1 \mathbf{E}_2 \cos[(\omega_1 + \omega_2)t] + \mathbf{E}_1 \mathbf{E}_2 \cos[(\omega_1 - \omega_2)t]] \right] \end{aligned} \quad (2.5)$$

The output consists of a time independent DC term (optical rectification, OR) and four terms involving new frequencies (Figure 2.2):

$2\omega_1, 2\omega_2$ : Second Harmonic Generation (SHG)

$\omega_1 + \omega_2$ : Sum Frequency Generation (SFG)

$\omega_1 - \omega_2$ : Difference Frequency Generation (DFG)

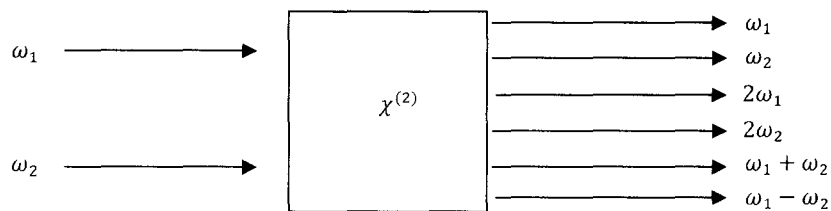


Figure 2.2 Geometry of two wave interaction

Theoretically, all the four nonzero frequency components should be present in the nonlinear polarization if there are two different frequency incident radiations. However, typically no more than one of these

components will be present in the nonlinear optical interactions. That is because the nonlinear polarization can efficiently generate an output radiation only if a certain phase-matching condition is satisfied, and usually this condition cannot be satisfied for more than one frequency component of the nonlinear polarization. The phase-matching condition will be discussed in the third section of this chapter.

SHG is the simplest three-wave mixing interaction. It can be treated as a special case of SFG, such that  $\omega_1 = \omega_2$ . In other words, there is only one incident radiation at frequency  $\omega$ . Then for the equation 2.5, the output only has the second harmonic term  $2\omega$  left. That is the reason why SHG is also called frequency doubling. Figure 2.2 shows the energy-level diagram describing SHG, two photons at frequency  $\omega$  are destroyed and one photon at frequency  $2\omega$  is simultaneously created in a single quantum-mechanical process. The whole process satisfies energy conservation. The solid and dashed lines represent the atomic ground state and virtual levels, respectively [36].

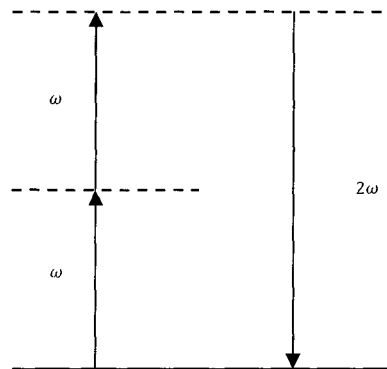


Figure 2.3 Energy-level diagram describing SHG [36]

Under proper SHG experimental conditions, nearly all of the incident radiation power can be converted to radiation at the second harmonic generation frequency. Moreover, SHG is commonly used as the first practical nonlinear frequency conversion process when developing a new nonlinear optical material or device. Preliminary SHG demonstrations also indicate a design's practicality for other conversion techniques such as difference and sum frequency generation or optical parametric oscillation and amplification.

## 2.2 Wave Equation and Coupled-Mode equation

In this section, we first examine how Maxwell's equations describe the generation of new frequency components of the field, and see how the various frequency components of the field become coupled by the nonlinear interaction. At first, we write Maxwell's equations in SI units as:

$$\nabla \cdot \mathbf{D} = \rho \quad (2.6)$$

$$\nabla \cdot \mathbf{B} = 0 \quad (2.7)$$

$$\nabla \times \mathbf{E} = -\frac{\partial \mathbf{B}}{\partial t} \quad (2.8)$$

$$\nabla \times \mathbf{H} = \mathbf{J} + \frac{\partial \mathbf{D}}{\partial t} \quad (2.9)$$

where  $\mathbf{E}$  is the electric field,  $\mathbf{H}$  is the magnetic field,  $\mathbf{D}$  is the electric flux density,  $\mathbf{B}$  is the magnetic flux density,  $\mathbf{J}$  is the free current density, and  $\rho$  is free charge density. Since we are dealing with a dielectric material, we have:

$$\mathbf{J} = 0 \quad (2.10)$$

$$\rho = 0 \quad (2.11)$$

we also assume that the material is nonmagnetic, so that:

$$\mathbf{B} = \mu \mathbf{H} = \mu_0 \mathbf{H} \quad (2.12)$$

where  $\mu$  is permeability of material and  $\mu_0$  is the permeability of free space.

Then we consider the nonlinear polarization:

$$\mathbf{D} = \varepsilon \mathbf{E} = \varepsilon_0 \varepsilon_r \cdot \mathbf{E} + \mathbf{P} \quad (2.13)$$

where  $\varepsilon$  is the permittivity,  $\varepsilon_0$  is the permittivity of free space,  $\varepsilon_r$  is the relative permittivity.

Taking the curl of both side of equation (2.8):

$$\nabla \times \nabla \times \mathbf{E} = -\frac{\partial}{\partial t} (\nabla \times \mathbf{B}) \quad (2.14)$$

Combing equations (2.9), (2.10), (2.12), and (2.14), we can get the following equation:

$$\nabla \times \nabla \times \mathbf{E} = -\mu_0 \frac{\partial^2}{\partial t^2} \mathbf{D} \quad (2.15)$$

Using (2.13) and vector identity ( $\nabla \times \nabla \times \mathbf{E} = \nabla \nabla \cdot \mathbf{E} - \nabla^2 \mathbf{E}$ ) in the case of no sources ( $\nabla \cdot \mathbf{E} = 0$ ), we can get the inhomogeneous optical wave equation under the slowly varying amplitude approximation is derived as:

$$\left( -\nabla^2 + \frac{1}{c^2} \frac{\partial^2}{\partial t^2} \right) \mathbf{E}(\mathbf{r}, t) = -\mu_0 \frac{\partial^2}{\partial t^2} \mathbf{P}(\mathbf{r}, t) \quad (2.16)$$

where the polarization vector  $\mathbf{P}$  is often split into its linear and nonlinear parts as:

$$\mathbf{P}(\mathbf{r}, t) = \mathbf{P}^{(1)}(\mathbf{r}, t) + \mathbf{P}^{NL}(\mathbf{r}, t) \quad (2.17)$$

Both  $\mathbf{E}(\mathbf{r}, t)$  and  $\mathbf{P}(\mathbf{r}, t)$  can be decomposed into a set of finite plane waves:

$$\mathbf{E}(\mathbf{r}, t) = \sum_n \mathbf{E}_n e^{-i(\omega_n t - \mathbf{k}_n \cdot \mathbf{r})} \quad (2.18)$$

$$\mathbf{P}^{(1)}(\mathbf{r}, t) = \sum_n \chi^{(1)}(\omega_n) \cdot \mathbf{E}_n(\omega_n, \mathbf{k}_n) \quad (2.19)$$

$$\mathbf{P}^{NL}(\mathbf{r}, t) = \sum_n \mathbf{P}^{NL}(\mathbf{r}) e^{-i(\omega_n t - \mathbf{k}_n \cdot \mathbf{r})} \quad (2.20)$$

where  $\mathbf{E}_n$  is the spatially slowly varying amplitude of the electric field.

Substituting (2.17), (2.18), (2.19) and (2.20) into (2.16), the wave equation now becomes as:

$$\left(-\nabla^2 + \frac{\omega_n^2}{c^2}\right)\mathbf{E}_n = -\mu_0\omega_n^2\mathbf{P}^{NL} \quad (2.21)$$

then, for  $n$  fields  $\mathbf{E}$ , there should be a set of  $n + 1$  couple wave equations.

In a second order nonlinear process, we only focus on the second order polarization, which is given in the form as:

$$\mathbf{P}^{(2)} = \varepsilon_0\chi^{(2)}\mathbf{E}^2 \quad (2.22)$$

In the technical literatures, rather than  $\chi^{(2)}$ , it is more common to see the 'nonlinear coefficient'  $d$ , which is defined as

$$d = \frac{\chi^{(2)}}{2} \quad (2.23)$$

Then, for the SHG process, the component of the second order polarization can be written as:

$$\mathbf{P}_\omega^{(2)} = 2d\varepsilon_0\mathbf{E}_{2\omega}\mathbf{E}_\omega^* \quad (2.24)$$

$$\mathbf{P}_{2\omega}^{(2)} = d\varepsilon_0\mathbf{E}_\omega^2 \quad (2.25)$$

then we can reach the following coupled mode equations for SHG process:

$$\frac{\partial\mathbf{E}_\omega(z)}{\partial z} = -i\kappa^*\mathbf{E}_{2\omega}(z)\mathbf{E}_\omega^*(z)e^{-i\Delta kz} \quad (2.26)$$

$$\frac{\partial\mathbf{E}_{2\omega}(z)}{\partial z} = -i\kappa\mathbf{E}_\omega(z)\mathbf{E}_\omega^*(z)e^{i\Delta kz} \quad (2.27)$$

where  $\Delta k$  is the phase velocity mismatch due to material dispersion, which is defined as:

$$\Delta k = k_{2\omega} - 2k_\omega = \frac{4\pi}{\lambda_\omega}(n_{2\omega} - n_\omega) \quad (2.28)$$

where  $k_{2\omega}$  and  $k_\omega$  are the propagation constants of pump and SHG light.

The parameter  $\kappa$  is the coupling coefficient for the SHG process, which is defined in the form of:

$$\kappa = \varepsilon_0 d_{eff} \sqrt{\frac{(2\omega)^2}{2n_\omega^2 n_{2\omega} A_{eff}} \left(\frac{\mu_0}{\varepsilon_0}\right)^{\frac{3}{2}}} \quad (2.29)$$

where,  $\varepsilon_0$  and  $\mu_0$  is the permittivity and permeability of free space, respectively,  $n_\omega$  and  $n_{2\omega}$  are the refractive index of pump and SHG light.  $A_{eff}$  is the effective area. In waveguide devices, it is convenient to assume the  $A_{eff}$  close to the area of guided mode profiles.  $d_{eff}$  is the effective SHG coefficient. When we assume the interaction optical beam having uniform cross sections in a homogeneous medium,  $d_{eff}$  can be considered equalling nonlinear coefficient  $d$ .

With boundary condition:  $E_\omega(0) = E_0$  and  $E_{2\omega}(0) = 0$ , where  $E_0$  is the amplitude of the incident pump light, the coupled-mode equations (2.26) and (2.27) can be solved under two different assumptions.

1) *Pump nondepletion solution:* If the conversion efficiency is low, therefore there is a very small depletion of the pump light power. We can approximate that  $E_\omega(z) = E_0$ . Then, combining the coupled-mode equations (2.26) and (2.27), we can get:

$$E_{2\omega}(z) = -i\kappa E_0^2 \exp\left(\frac{i\Delta kz}{2}\right) \left(\frac{\sin\Delta kz/2}{\frac{\Delta kz}{2}}\right) \quad (2.30)$$

$$P_{2\omega}(z) = \frac{8\pi^2}{n_\omega^2 n_{2\omega} \lambda_\omega^2 c \epsilon_0} d_{eff}^2 z^2 \frac{\sin^2(\Delta kz/2)}{(\Delta kz/2)^2} \frac{P_\omega^2(0)}{A_{eff}} \quad (2.31)$$

and the SHG conversion efficiency is defined as:

$$\eta = \frac{P_{2\omega}(z)}{P_\omega(0)} = \frac{8\pi^2}{n_\omega^2 n_{2\omega} \lambda_\omega^2 c \epsilon_0} d_{eff}^2 L^2 \frac{\sin^2(\Delta kz/2)}{(\Delta kz/2)^2} \frac{P_\omega(0)}{A_{eff}} \quad (2.32)$$

The normalized conversion efficiency  $\eta_{nor}$ , another commonly used parameter to represent the conversion performance, is given in the form as:

$$\eta_{nor} = \frac{P_{2\omega}(L)}{P_\omega^2(0)L^2} = \frac{8\pi^2}{n_\omega^2 n_{2\omega} \lambda_\omega^2 c \epsilon_0} d_{eff}^2 \frac{\sin^2(\Delta kz/2)}{(\Delta kz/2)^2} \frac{1}{A_{eff}} \quad (2.33)$$

It is only depends on the nonlinear properties of the medium and the overlap of the interacting waves.

2) *Pump depletion solution*: If the conversion efficiency is high enough that the pump amplitude cannot be treated as a constant. The coupled-mode equations (2.26) and (2.27) must be solved with the boundary condition ( $E_\omega(0) = E_0, E_{2\omega}(0) = 0$ ) and the power conservation relation:

$$\frac{d}{dz} (|E_\omega(z)|^2 + |E_{2\omega}(z)|^2) = 0 \quad (2.34)$$

The equations were solved in previous literatures. The SHG output power under pump depletion assumption is given by:

$$P_{2\omega}(z) = P_\omega(0) \tanh^2 \left[ C \sqrt{\frac{P_\omega(0)}{A_{eff}}} z \right] \quad (2.35)$$

where

$$C = \frac{8\pi\omega d_{eff}}{c^2\sqrt{\epsilon}} \sqrt{\frac{2\pi c}{\sqrt{\epsilon}}} \quad (2.36)$$

This function is plotted in Figure 2.4. We can see that the conversion efficiency approaches 100% asymptotically with increasing the crystal length. As we discuss before, only at low conversion efficiency, power nondepletion assumption can be applied. From Figure 2.4, we can see that the low efficiency approximation is adequate to around 10% conversion efficiency.

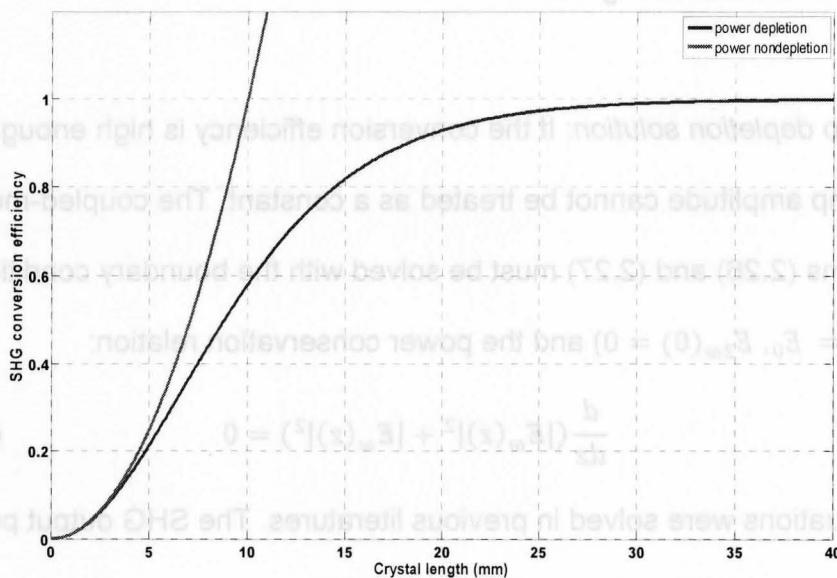


Figure 2.4 Dependence of SHG efficiency on interaction length under power depletion assumption (blue line) and power nondepletion assumption (green line)

## 2.3 Phase Matching

Equation (2.32) shows all the factors which will affect the SHG output power. Apparently, using longer devices based on higher second nonlinear coefficient and confining the incident beam and generated beam within a small cross-section area will lead to higher SHG conversion efficiency. Moreover, the major factor affecting the output power shown in (2.32) is the wavevector mismatch  $\Delta k = k_{2\omega} - k_{\omega} = \frac{4\pi}{\lambda_{\omega}}(n_{2\omega} - n_{\omega})$ , which is called the phase matching condition. It is easy to draw the relationship between SHG conversion efficiency and phase mismatch (Figure 2.5).

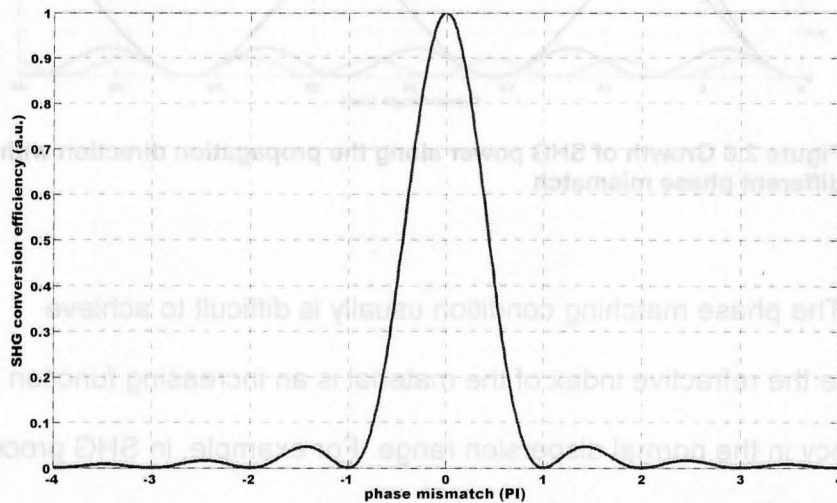
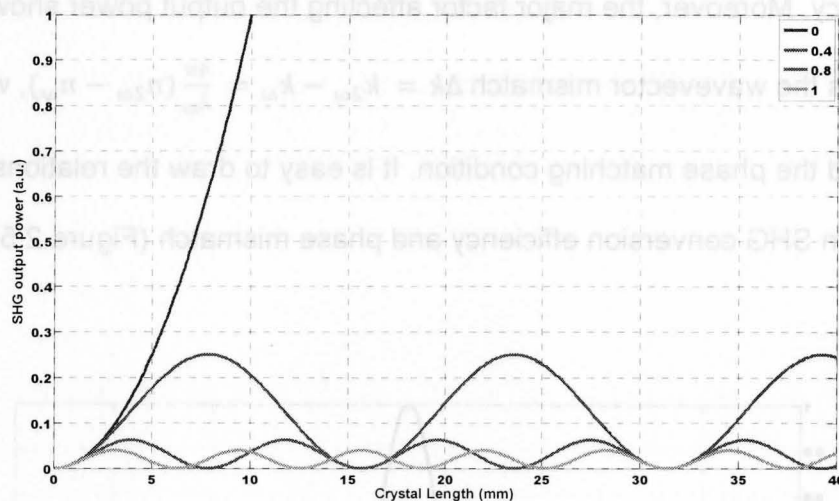


Figure 2.5 Effects of phase mismatch on the SHG conversion efficiency

Obviously, only when the  $\Delta k = 0$ , or perfect phase matching, will the output power achieve the maximum value. In the meantime, on the wave

propagation direction, SHG power can continuously increase only when the phase is perfectly matched. Otherwise, the SHG output power oscillates between zero and its maximum value, which leads to a dramatic decrease in the conversion efficiency (Figure 2.6).



**Figure 2.6 Growth of SHG power along the propagation direction with different phase mismatch**

The phase matching condition usually is difficult to achieve because the refractive index of the material is an increasing function of frequency in the normal dispersion range. For example, in SHG process, to satisfy phase matching condition,  $n_{2\omega}$  and  $n_{\omega}$  has to be equal, which is impossible while  $2\omega > \omega$ . In principle, it is possible to achieve the phase-matching condition by making use of abnormal dispersion, in which the decrease in refractive index with increasing frequency occurs near an

absorption feature [36]. However, the most typical method for achieving phase matching is to make use of the birefringence property of many nonlinear optical crystals.

Birefringence is the dependence of the refractive index on the direction of polarization of the light. By carefully choosing the polarizations of fundamental light and generated light, the phase matching condition will be satisfied.

For instance, in a negative uniaxial crystal, the category which most common nonlinear optical crystals belong to, the extraordinary axis has a smaller refractive index than the ordinary axes. Then, to achieve the phase matching condition for SHG process, we have two methods:

$$n_e(2\omega) = n_o(\omega) \quad (2.37)$$

$$\mathbf{E}_o(\omega) + \mathbf{E}_o(\omega) \rightarrow \mathbf{E}_e(2\omega) \quad (2.38)$$

or

$$n_e(2\omega) = \frac{1}{2}[n_o(\omega) + n_e(\omega)] \quad (2.39)$$

$$\mathbf{E}_o(\omega) + \mathbf{E}_e(\omega) \rightarrow \mathbf{E}_e(2\omega) \quad (2.40)$$

the condition specified by equations 2.37 & 2.38 is called “Type-1 phase matching” and the condition given by 2.39 & 2.40 is called “Type-2 phase matching”. BPM is usually achieved by a method called angle tuning. This method involves precise angular orientation of the crystal with respect to the propagation direction of the incident light. However, the angle tuning method has one serious drawback. If there is an angle with any value

other than 0 or 90 degree between the propagating direction of extraordinary wave and the optical axis, the Poynting vector  $\mathbf{S}$  and the propagation vector  $\mathbf{k}$  will not be parallel. As a result, the ordinary and extraordinary rays with parallel propagation vectors will quickly diverge from each other. This walk-off effect decreases the overlap of fundamental waves and generated waves, which limits the nonlinear optical conversion efficiency.

For some crystals, the amount of birefringence is strongly temperature-dependent. As a result, it is possible to achieve phase matching in these crystals by controlling the device at a certain temperature. This method is called temperature tuning.

BPM methods are limited by many factors, such as angle, wavelength and temperature. There is another method known as quasi-phase matching (QPM) that can be used to achieve phase matching. The idea of QPM was first proposed by Armstrong in 1962 [37]. But there was no practical technique to realize QPM for wavelength conversion until 1980's [38].

QPM does not depend on birefringence of materials, but instead, on creating a periodic domain inverse structure in the nonlinear optical material. This periodic domain inverse structure periodically inverts one of the crystalline axes, often the optical axis of a ferroelectric material. This inversion leads the sign of the nonlinear coupling coefficient  $d_{eff}$  ( $d_{eff} =$

$\chi^{(2)}/2$ ) periodically inverting. The inversion period  $\Lambda$  is carefully chosen as twice of the coherent length  $l_c$  ( $l_c = \frac{\pi}{\Delta k}$ ). Thus, each time the amplitude of generated electric field is about to decrease due to the phase mismatch, the reversal of the sign of polarization occurs which allows the amplitude to continue increasing. Through this mean, the nonzero wavevector mismatch can be compensated. Figure 2.7 illustrates the comparison effect of three phase matching conditions.

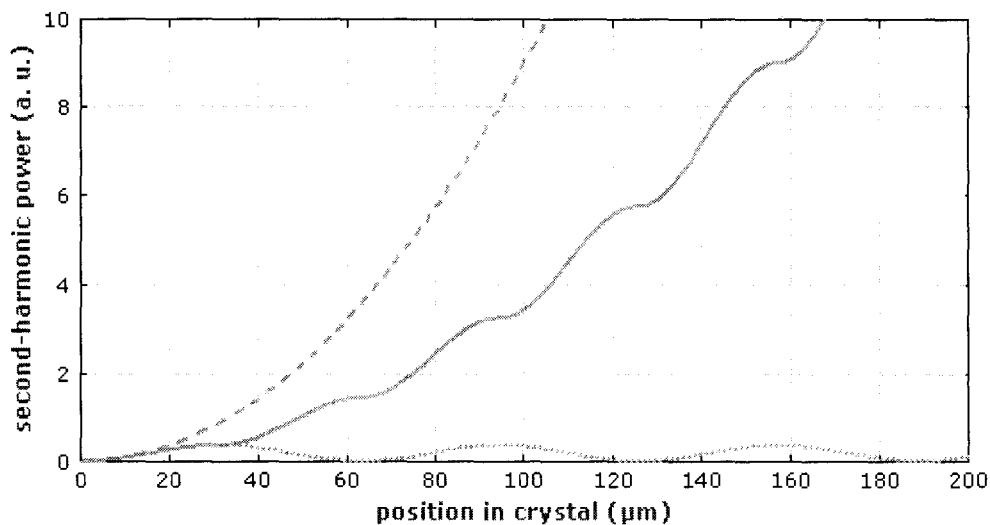


**Figure 2.7 Growth of second-harmonic power in a nonlinear crystal with phase matching (dashed curve), without phase matching (dotted curve), and with quasi-phase matching (solid curve)** ([http://www.rp-hotonics.com/quasi\\_phase\\_matching.html](http://www.rp-hotonics.com/quasi_phase_matching.html), accessed Sept. 2008)

Compared to other phase matching methods, QPM technique has many advantages. Table 2.1 shows a brief comparison between QPM and BPM. Although the conversion efficiency of QPM is theoretically lower

than the perfect phase matching, using QPM technique usually dramatically enhances the conversion efficiency in practical applications because QPM can use the largest nonlinear coefficient while usually it is impossible for BPM. Moreover there is no limitation for QPM method, so wavelength conversion in the whole transparent window of the crystal can be achieved simply by choosing the appropriate QPM structure period.

<b>Quasi-Phase Matching</b>	<b>Birefringent Phase Matching</b>
Noncritical phase matching, no walkoff	Mostly critical phase matching, walkoff
Larger diagonal nonlinear coefficients can be used	Only smaller, non-diagonal coefficients can be used
Phase matching any wavelength combinations within crystal transparency	Limited phase matching wavelength (e.g. no blue SHG for LiNbO <sub>3</sub> )
Tuning via temperature, multiple or continuous fan-out type grating periods	Tuning via temperature and angle
Wide acceptance bandwidth/angle, easy to align	Limited acceptance bandwidth/angle, difficult to align
User design friendly criteria	

**Table 1.1 Comparison of QPM and BPM**

A number of different technologies have been developed for the fabrication of quasi-phase matched structure in past decades, including direct writing by electron beams, titanium indiffusion, electric-field poling

and techniques based on wafer bonding [39]. Some of them are already matured and cost efficient. The detail of the fabrication of QPM structure will be introduced in next chapter.

## 2.4 Properties of Lithium Niobate

Due to the emerging demands of wavelength conversion devices in many science and engineering fields, many nonlinear optical crystals that can be used to obtain high efficient conversion, such as Lithium Niobate ( $\text{LiNbO}_3$ ), Beta Barium Borate (Beta- $\text{BaB}_2\text{O}_4$  / BBO), Potassium Titanium Oxide Phosphate ( $\text{KTiOPO}_4$  / KTP), Lithium Triborate ( $\text{LiB}_3\text{O}_5$  / LBO), Potassium Dihydrogen Phosphate (KDP), and Lithium Tantalate ( $\text{LiTaO}_3$ ), have been developed. Among them,  $\text{LiNbO}_3$ , often referred to as “the silicon of nonlinear optics,” is one of the most versatile and well-developed nonlinear optical materials (Figure 2.8). The basic material properties of  $\text{LiNbO}_3$  are very promising for practical applications. Lithium niobate, which is not present in the nature, is permitted to grow in quite large crystals by mature and low cost techniques. It is already produced at a volume of over 100 tons per year. In other words, this is a non expensive starting material for devices.

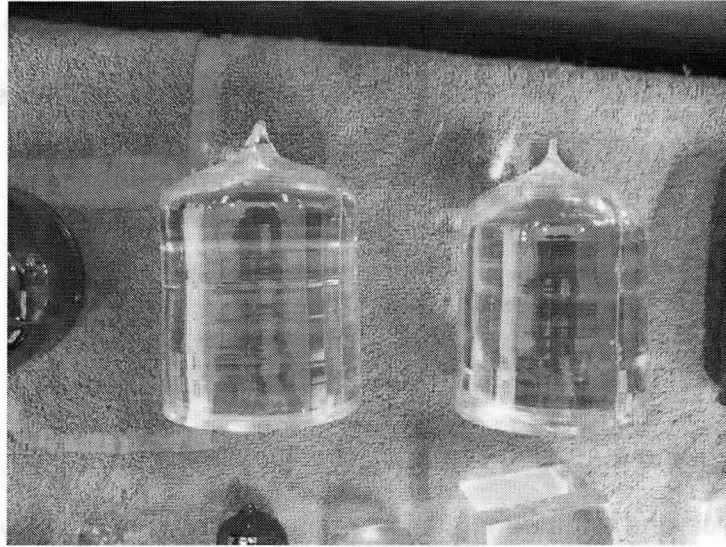


**Figure 2.8 Lithium Niobate Crystal**  
 (<http://physics.nankai.edu.cn/grzy/zhangl/english/prod01.htm>, accessed Sept. 2008)

---

General Properties:

melting point:	1260 °C
crystal symmetry:	trigonal, point group 3m
hardness	5 Mohs
stoichiometry	nonstoichiometric, ~6% Li deficiency easy to dope in high concentration
ferroelectricity	Curie temperature $T_C = 1150\text{ °C}$ Spontaneous polarization $P_S(\text{RT}) \sim 96\text{ C/m}^2$ 180° domains

---

Optical related properties:

transparency region	VIS/NIR (~350 nm to ~5 μm)
optical anisotropy	uniaxial, c-axis
refractive indices	$n_o = 2.286$ , $n_e = 2.203$ (632.8 nm)
optical homogeneity	
optical effects	acousto-optic, electro-optic second order nonlinearity bulk photovoltaic effect photorefractive effect

---

**Table 2.2 Basic properties of lithium niobate crystal [40, 41]**

Lithium niobate is a solid crystalline material, which is chemically very stable at room temperature and quite stable to environmental humidity. Single crystals of this material were first fabricated by using the Czochralski technique of pulling from the melt by Ballman in 1965. To date, the crystal growth industry is able to provide very homogeneous crystals of several kilograms and three or four inches in diameter. Table 2.1 shows a summary of the main properties of the lithium niobate crystal. It is a ferroelectric material below a very high Curie temperature (ferroelectrics are materials exhibiting a spontaneous electric dipole moment, analogous to magnetic dipoles in ferromagnetic material). The combination of excellent electro-optical, acoustic-optical and non-linear optical properties makes  $\text{LiNbO}_3$  an attractive host material for various useful applications. It is used mostly in radio frequency surface acoustic wave filters due to its large piezoelectric coefficient. The electro-optic effect, with moderately high coefficient, is a very useful property when manufacturing of high-speed digital modulators for telecommunication systems. The pure material is transparent from the band gap edge absorption at about 320 nm ( $\sim 3.9$  eV) up to the first infrared vibrational absorptions at a wavelength of about 5  $\mu\text{m}$  (0.25 eV) providing low loss for all UV, visible and mid-infrared light propagating, which is very important for photonic applications.

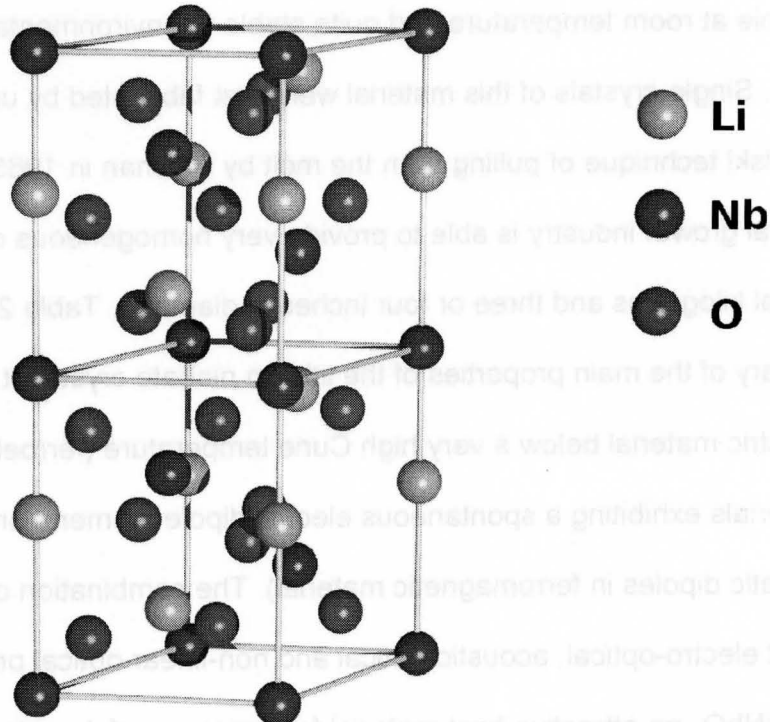


Figure 2.9 Hexagonal crystal structure of  $\text{LiNbO}_3$  [42]

The crystalline structure of this material at room temperature corresponds to the trigonal  $3m$  point group (Figure 2.9) [42]. The crystal is optically uniaxial, with two refractive indices: ordinary and extraordinary. Both indices have values larger than two over the entire transparency window, which makes it necessary to fit antireflection coating layers on the optical surfaces in many cases.

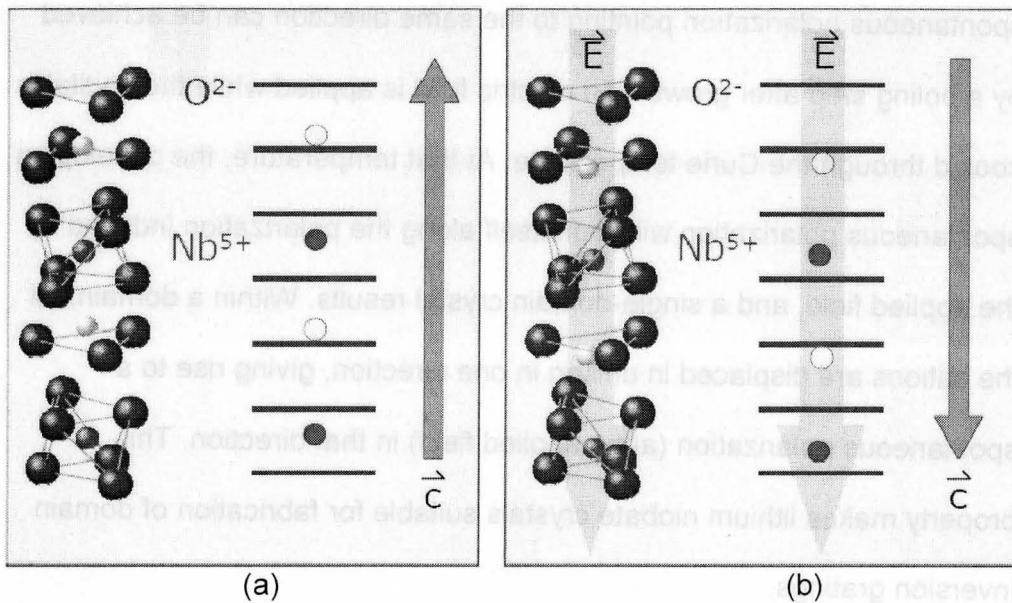


Figure 2.10 (a) para-electric phase of  $\text{LiNbO}_3$  (b) ferro-electric phase of  $\text{LiNbO}_3$  [43]

As most of niobium oxides, lithium niobate belong to the ferroelectrics. In the high temperature (para-electric) phase, the crystal has inversion symmetry (Figure 2.10 (a)). When the crystal is cooled below the phase transition temperature, or Curie temperature, it undergoes a phase transition to the ferro-electric phase (Figure 2.10 (b)). Consequently, no further phase transition is observed below the Curie temperature, and there is no structural mismatch between neighbouring domains. As shown in Figure 2.10, in the lithium niobate crystal structure, the oxygen planes are represented by lines with the cations between the plans. The cations are displaced from the center position, defining the direction of the polar Z-axis. The phase transition is caused by the different displacement of the cations. Thus, a uniform crystal with a

spontaneous polarization pointing to the same direction can be achieved by a poling step after growth. An electric field is applied while the crystal is cooled through the Curie temperature. At that temperature, the developing spontaneous polarization will align itself along the polarization induced by the applied field, and a single-domain crystal results. Within a domain, all the cations are displaced in unison in one direction, giving rise to a spontaneous polarization (at no applied field) in that direction. This property makes lithium niobate crystals suitable for fabrication of domain inversion gratings.

## 2.5 Temperature Dependence of QPM-LiNbO<sub>3</sub>

As one of the most widely used nonlinear optical crystal, LiNbO<sub>3</sub> is highly temperature dependent. This feature is useful in some applications but also limits the devices' performance. A Sellmeier equation for the extraordinary refractive index of congruent LiNbO<sub>3</sub> was derived by Jundt for theoretically modelling the temperature dependence [44]. The equation is in the form as:

$$n_e^2 = a_1 + b_1f + \frac{a_2 + b_2f}{\lambda^2 - (a_3 + b_3f)^2} + \frac{a_4 + b_4f}{\lambda^2 - a_5^2} - a_6\lambda^2 \quad (2.41)$$

Table 2.3 shows the values of the parameters in Sellmeier equation:

Parameter	Value
$a_1$	5.35583
$a_2$	0.100473
$a_3$	0.20692
$a_4$	100
$a_5$	11.34927
$a_6$	$1.5334 \times 10^{-2}$
$b_1$	$4.629 \times 10^{-7}$
$b_2$	$3.862 \times 10^{-8}$
$b_3$	$-0.89 \times 10^{-8}$
$b_4$	$2.657 \times 10^{-5}$

**Table 2.3 Parameters of Sellmeier equation [44]**

For the temperatures expressed in degrees Celsius, the temperature parameter is given by:

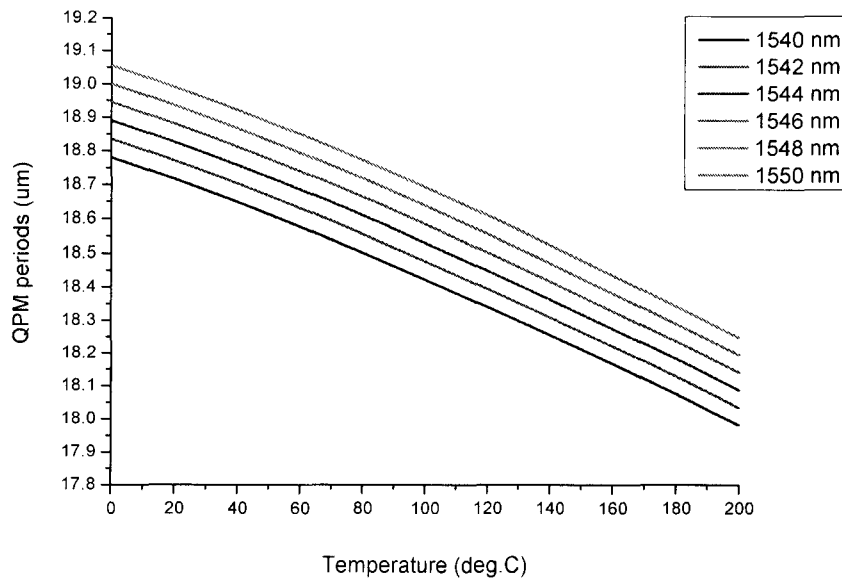
$$f = (T - T_0)(T + T_0 + 2 \times 273.16) = (T - 24.5)(T + 570.82) \quad (2.42)$$

For calculating the QPM period  $\Lambda$ , the linear thermal expansion at temperature  $T$  should also be considered as:

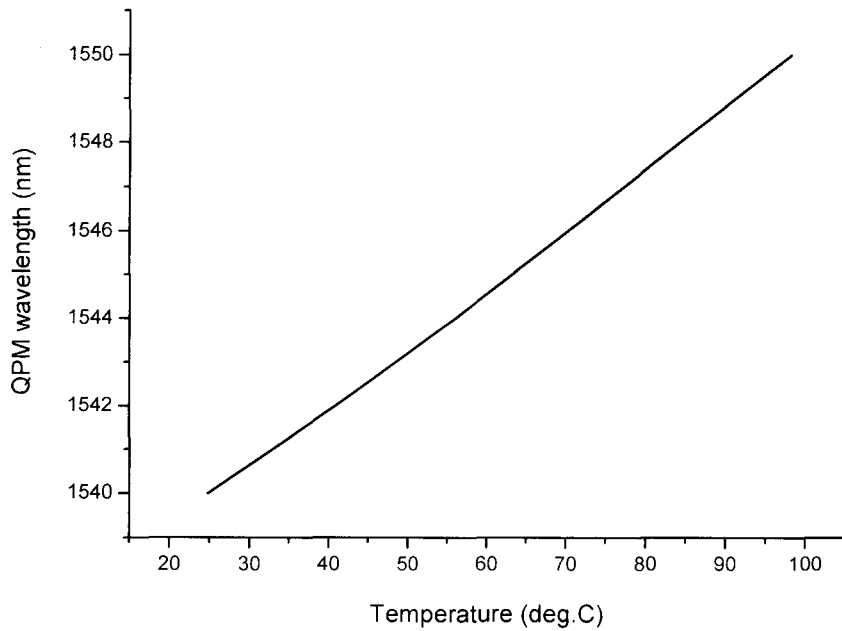
$$\Lambda(T) = \Lambda_0 + \alpha(T - T_0)\Lambda_0 \quad (2.43)$$

where  $\alpha$  is the thermal expansion coefficient of congruent LiNbO<sub>3</sub>.

Combining (2.41), (2.42) and (2.43), we can obtain the relationship between the QPM period  $\Lambda$ , wavelength  $\lambda$  and temperature  $T$  shown in Figure 2.11.



(a)



(b)

Figure 2.11 Temperature dependence of the QPM period (a) and wavelength (b)

As shown in Figure 2.11, for a certain QPM wavelength, the QPM period decreases as temperature increase. For a fixed QPM period, the QPM wavelength increases as temperature increase. The simulation results indicate that the temperature sensitivity of the QPM wavelength is about  $0.137 \text{ nm}/^{\circ}\text{C}$  for a congruent PPLN device with a period of  $18.7 \text{ }\mu\text{m}$ , which means about 10 nm wavelength tuning can be achieved by tuning temperature from room temperature ( $\sim 25 \text{ }^{\circ}\text{C}$ ) to  $100 \text{ }^{\circ}\text{C}$ .

## CHAPTER 3

### MICRO-HEATER DESIGN AND WAVEGUIDE MODE PROFILE

#### 3.1 Micro-Heater Design

Heat can be defined as energy in transit. The transfer of heat is always from a high-temperature object to a lower-temperature object. The object with higher-temperature transfers energy to the lower-temperature object, which increases its internal energy – this is called heating. Usually there are three modes of heat transfer, or energy transfer: conduction, convection and radiation [45, 46].

Conduction refers to heat transfer by diffusion through a solid material or non-moving fluid. It is analogous to electrical conduction. When there is a temperature gradient in a body, then the heat (energy) will flow from the hotter part to the colder region because the higher speed particles collide with the slower ones with a net transfer of energy to the slower ones. According to Fourier's Law:

$$H = \frac{\Delta Q}{\Delta t} = \frac{\kappa A \Delta T}{d} \quad (3.1)$$

where  $H$  is the rate of heat flow in Watt which is also called heat flux,  $\Delta Q$  is the quantity of heat transferred in Joules,  $\kappa$  is the thermal conductivity (W/mK),  $A$  is the total cross sectional area through which heat transfer

takes place ( $m^2$ ),  $\Delta T = T_{hot} - T_{cold}$  is the temperature difference of two part (K), and  $d$  is the thickness of barrier (m). Just like the definition of the “current” in electronics, heat flux is the heat flowing across a unit area per unit time.

Another mechanism for heat transfer is convection. It refers to heat transfer by mass motion of a fluid such as gas or water. There are two types of convection: free and forced. The free convection occurs because a high temperature fluid expands and becomes less dense and rises while the more dense cold part descends and patterns of circulation can be formed. On the other hand, an external pump can drive the fluid to transfer heat from one part to another. This is called “forced convection”.

Radiation is heat transfer by the emission of electromagnetic waves which carry energy away from the emitting object. Thermal radiation waves are usually in the infrared region for objects of ordinary temperatures. Every body can exchange heat by emitting or absorbing thermal radiation. This process can be evaluated using the Stefan-Boltzmann law:

$$P_{net} = e\sigma A(T^4 - T_c^4) \quad (3.2)$$

where  $P_{net}$  is the net radiated power,  $e$  is the emissivity coefficient,  $\sigma$  is the Boltzmann constant,  $A$  is the radiation area,  $T$  is the temperature of the radiator, and  $T_c$  is the environment temperature.

For our device, conduction is studied as the only mode for heat transferring. This is a valid assumption because convection and radiation heat transfer can be neglected. As a solid device using in a stable environment, there is no sufficient fluid medium convection. As well, using a simple calculation with equation 3.2, we can estimate that the radiation power of our heater structure design is less than one milli-Watt, which is negligible compared with several Watt total heat generation.

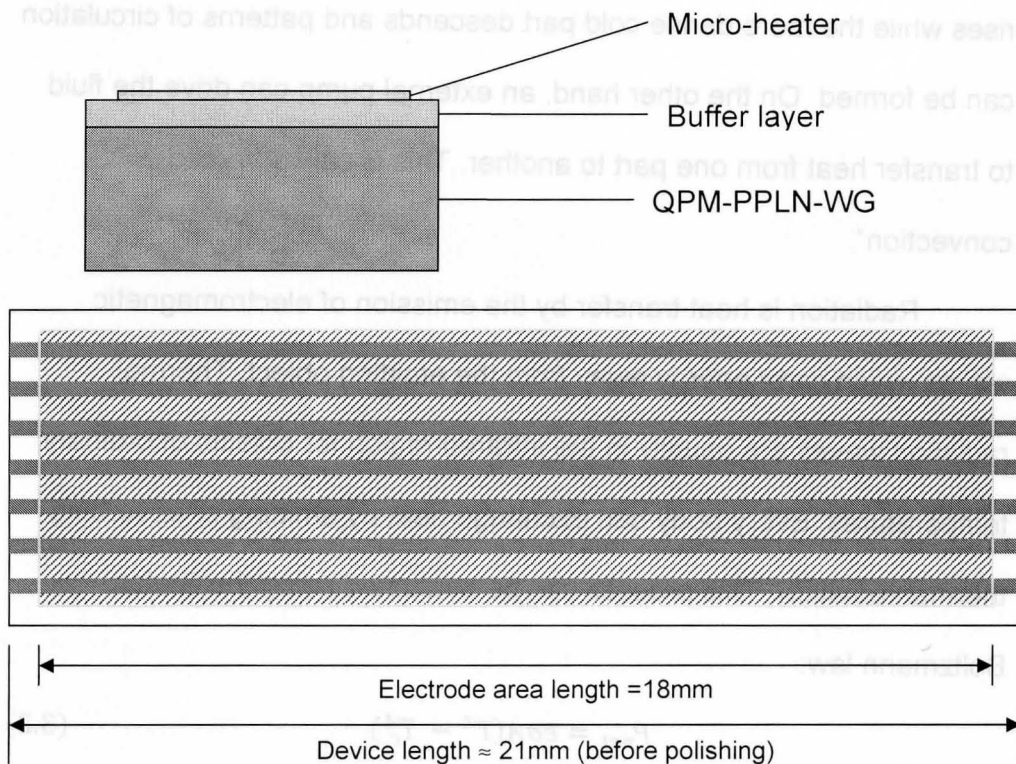


**Figure 3.1 Device structure diagram**

Figure 3.1 shows the schematic diagram of our device structure. The conventional PPLN waveguide device is covered by a polymer buffer layer and a micro resistance heater based on Au/Pt/Cr triple layers is fabricated on the top. The length of the heater area is about 18 mm and the thicknesses of three metal layers are: 30 nm of chromium, 250 nm of platinum and 150 nm of gold. Platinum is selected as the heater material because of its good thermal conductivity, low resistivity, and high melting point. The chromium layer acts as an adhesion layer for the platinum layer attachment to the lithium niobate surface. The gold layer on the top is just for better Ohmic contact. The resistance is mainly influenced by the platinum layer's thickness because the resistance of gold layer can be neglected and the chromium layer is thought mainly to be the Cr-oxide which is formed during the evaporation. The buffer layer has two functions: separating the metal layer and LiNbO<sub>3</sub> waveguide to avoid any possible light leaking, and improving the uniformity of the heat distribution.

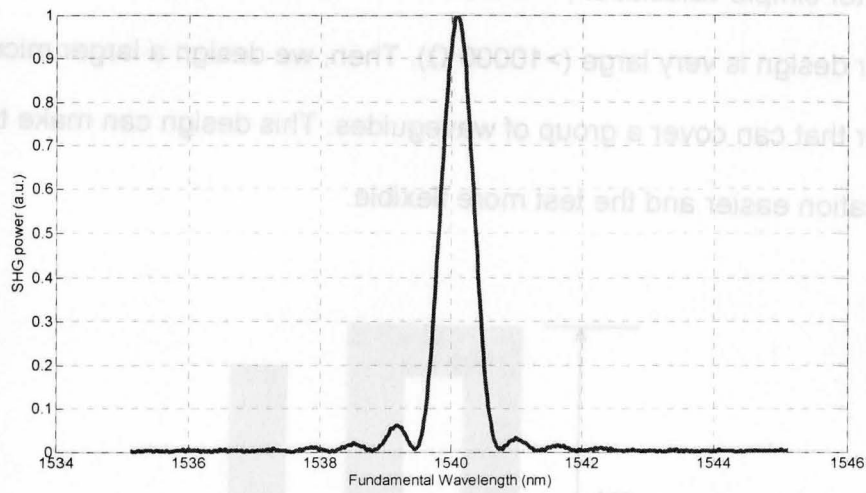
Several heater designs have been examined. The straight line structure is designed and fabricated at first. Figure 3.2 shows the top view of the straight line micro-heater: the blue line is the waveguide and red rectangle is the micro-heater. The waveguide width is 9 μm and the micro-heater width is 15 μm. The resistance of the heater can be calculated as:

$$R_{Pt} = \frac{\rho L}{A} = \frac{1.1 \times 10^{-7} \times 0.018}{15 \times 10^{-6} \times 250 \times 10^{-9}} = 528 \Omega \quad (3.3)$$

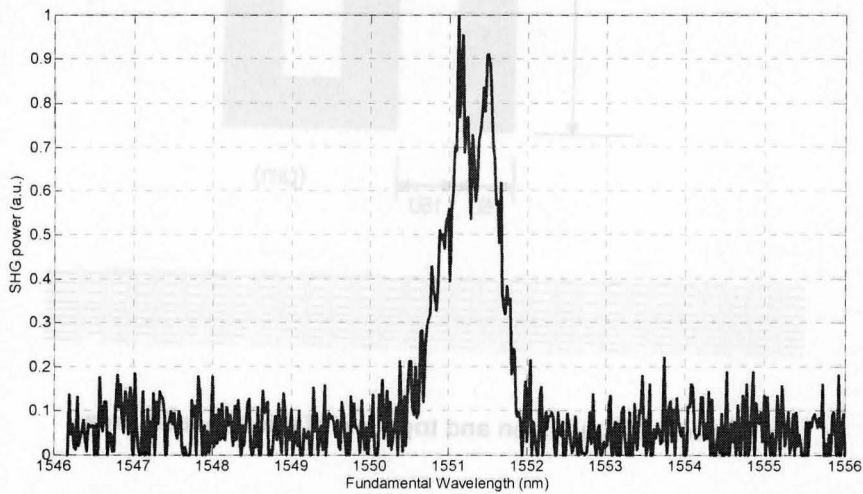


**Figure 3.2 Straight line micro-heater**

But when we test the device's performance, we find that the heat distribution of this micro-heater structure is non-uniform. We draw this conclusion by comparing the SHG tuning curves before and after applying the current into the micro-heater (Figure 3.3). The SHG tuning curve without current injection is a Sinc function curve which is almost perfect match with the theoretical simulation. But the SHG tuning curve with certain current applied into the micro-heater is rough and multi-peaks, which indicates that the temperature is non-uniform along the waveguide. After examining the device under the microscope, we believe that this problem is caused by the misalignment between the heater and the waveguide. It is hard to precisely align the heaters with the waveguides during the lithograph process since the waveguides are transparent.



(a)



(b)

**Figure 3.3 SHG tuning curve without current injection (a) and with current injection (b)**

To overcome this problem, a square wave shape micro-heater is designed to make the heater area more uniform (Figure 3.4).



**Figure 3.4 Square wave micro-heater**

But after simple calculation, we find that the resistance of this micro-heater design is very large ( $>10000 \Omega$ ). Then, we design a larger micro-heater that can cover a group of waveguides. This design can make the fabrication easier and the test more flexible.

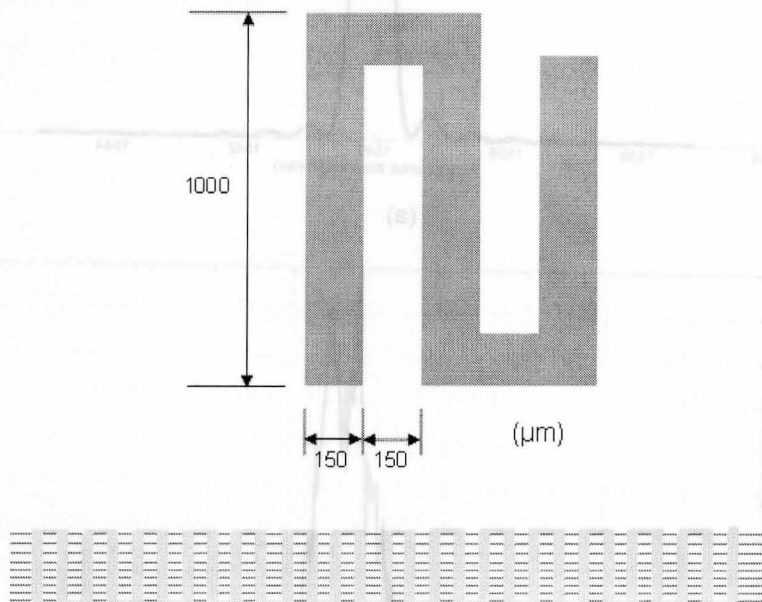


Figure 3.5 Dimension and top view of micro heater area

Figure 3.5 shows the dimension and top view of the periodic rectangular heater structure. The heater area covers a group of waveguides (blue lines in Figure 3.5). Then, the resistance of the heater can be calculated as:

$$R_{Pt} = \frac{\rho L}{A} = \frac{1.1 \times 10^{-7} \times 0.069}{150 \times 10^{-6} \times 250 \times 10^{-9}} = 202.4 \Omega \quad (3.4)$$

The operational principle of the heater is the Joule effect. The power of heat generated by the current flowing through a conductor can be expressed as:

$$P = V^2/R = I^2R \quad (3.5)$$

In our experiments, the current is applied by two probes from a Keithley 2400 source meter. The parasitic resistance of the source and probes is about  $0.5 \Omega$  then the power loss on the probes is less than 1%.

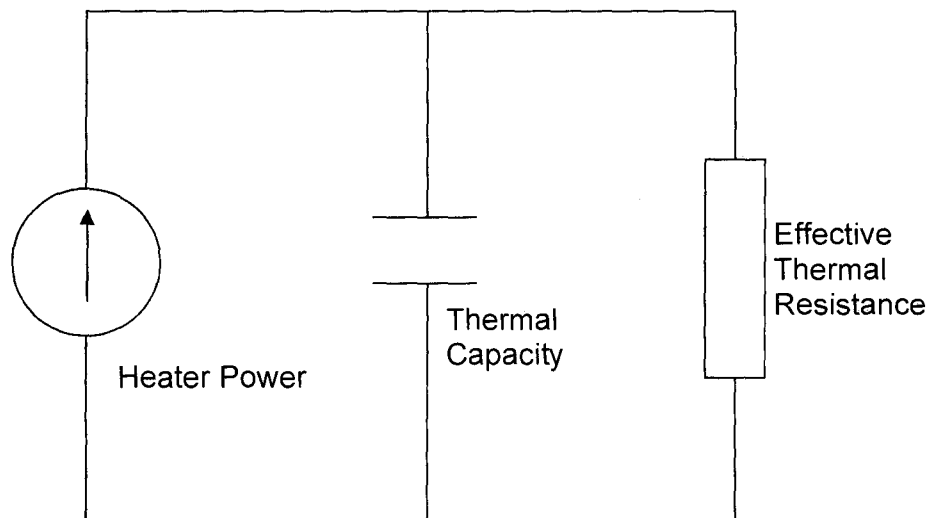


**Figure 3.6 Lumped Parameter Thermal Model for integration structure**

The simple lumped parameter thermal model of the integration structure is illustrated in Figure 3.6. The thermal circuit resistance is composed by three parts: thermal resistance of buffer layer, thermal resistance of  $\text{LiNbO}_3$ , and the spreading thermal resistance. The thermal

spreading resistance occurs when heat leaves a source of finite dimensions and enters a larger region. We treat the micro-heater area as a rectangular heat source (Figure 3.7). By using the simulation software provided by the Microelectronics Heat Transfer Laboratory in University of Waterloo, we can estimate the effective resistance  $R_{eff} = 50.47 \text{ K/W}$ .

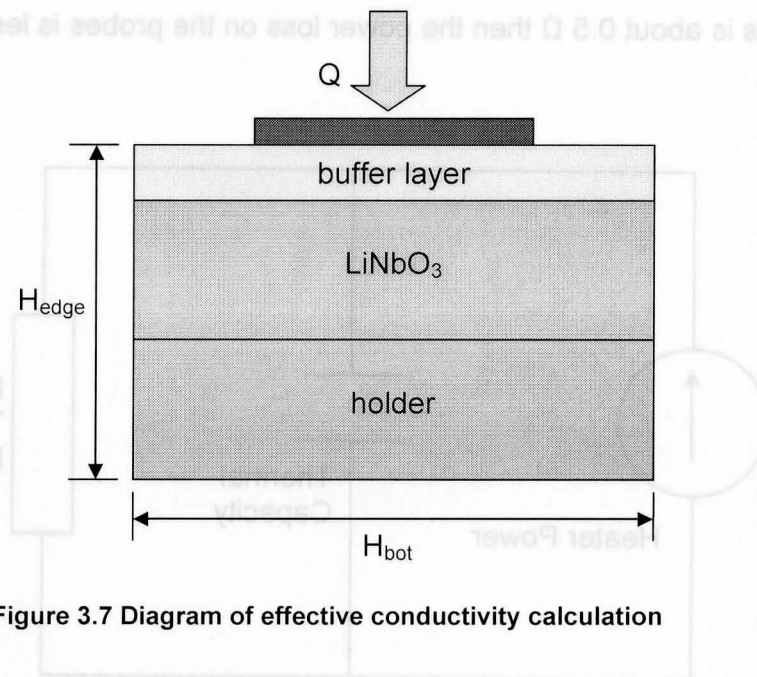


Figure 3.7 Diagram of effective conductivity calculation

Since

$$P = \frac{T_{heater} - T_{sub}}{R_{eff}} \quad (3.6)$$

and assuming temperature of substrate is room temperature. Then, by combining equation 3.5 and 3.6 we can reach a relationship between the injection current and temperature, which is shown in Figure 3.8.

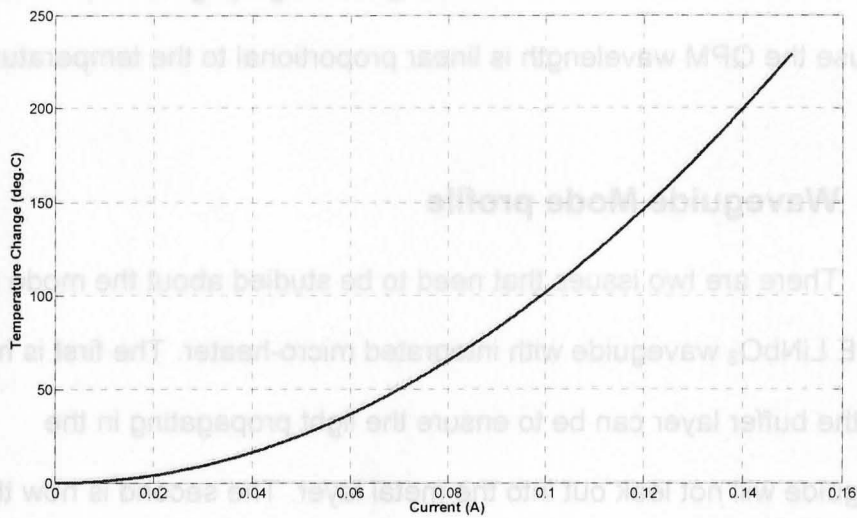


Figure 3.8 Temperature change versus current injection

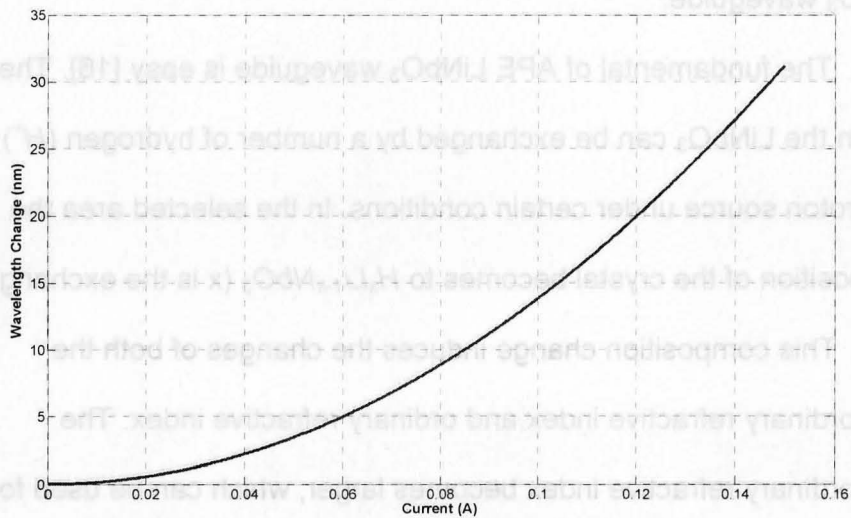


Figure 3.9 Current dependence of QPM wavelength change

Moreover, based on Sellmeier equation that we discussed in the Chapter 2, we can get the similar curve for the relationship between the

injection current and the QPM wavelength change (Figure 3.9). That is because the QPM wavelength is linear proportional to the temperature.

### 3.2 Waveguide Mode profile

There are two issues that need to be studied about the mode profile of APE LiNbO<sub>3</sub> waveguide with integrated micro-heater. The first is how thick the buffer layer can be to ensure the light propagating in the waveguide will not leak out into the metal layer. The second is how the buffer layer affects the mode profile compared with the normal APE LiNbO<sub>3</sub> waveguide.

The fundamental of APE LiNbO<sub>3</sub> waveguide is easy [16]. The  $Li^+$  ions in the LiNbO<sub>3</sub> can be exchanged by a number of hydrogen ( $H^+$ ) from the proton source under certain conditions. In the selected area the composition of the crystal becomes to  $H_xLi_{1-x}NbO_3$  ( $x$  is the exchange ratio). This composition change induces the changes of both the extraordinary refractive index and ordinary refractive index. The extraordinary refractive index becomes larger, which can be used for confining light wave. Since the ordinary refractive index becomes smaller after PE process, the PE waveguide can only guide the light polarized along the crystal axis. For z-cut LiNbO<sub>3</sub>, only transverse-magnetic <sup>TM</sup> modes can be guided. The following annealing process has to be applied

to improve the stability and enhance the propagation loss. The more detailed fabrication procedures will be introduced in the next chapter.

A lot of research work has been done to theoretically and experimentally characterize APE LiNbO<sub>3</sub> [47, 48, 49, 50]. As shown in Figure 3.10 (a), PE process induces a rectangular area under the surface with the refractive index change:

$$\Delta n_{PE} = \sqrt{a_1 + \frac{a_2}{\lambda^2 - a_3^2}} \quad (3.7)$$

where  $\lambda$  is wavelength in  $\mu\text{m}$ , and the value of parameters  $a_n$  are fit from experimental results.

The exchange width is approximately equal to the window width opening on the mask for lithographical process. The depth of PE waveguide  $d_{PE}$  depends on the process temperature and time. Their relationship can be described as:

$$d_{PE} = 2\sqrt{D_{PE}(T_{PE})t_{PE}} \quad (3.8)$$

$$D_{PE}(T_{PE}) = D_{PE0} \exp\left(-\frac{Q_{PE}}{\kappa T_{PE}}\right) \quad (3.9)$$

where  $D_{PE}(T_{PE})$  is a temperature dependent diffusion coefficient,  $D_{PE0}$  the diffusion constant,  $Q_{PE}$  is the activation energy, and  $\kappa$  is the Boltzmann's constant.

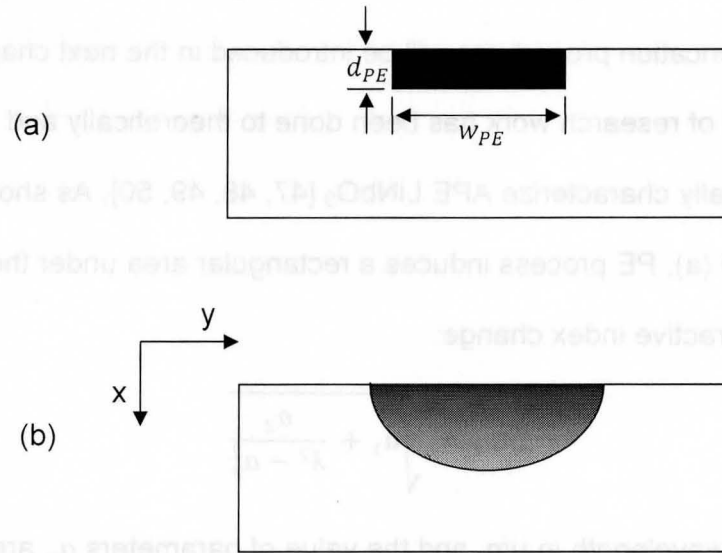


Figure 3.10 refractive index distributions in PE (a) and APE (b) waveguide

The thermal annealing process diffuses the protons to a deeper region from the surface, resulting in an extended graded index distribution and reduction of the maximum index change (Figure 3.10-(b)). This distribution can be described by the following diffusion equation [50]:

$$C(x, y) = \left( \frac{1}{\cosh^2 \left( \frac{2x}{d_x} \right)^b} \right) \times \left( \frac{1}{\cosh^2 \left( \frac{w+2y}{d_y} \right)^b + \cosh^2 \left( \frac{w-2y}{d_y} \right)^b} \right) \quad (3.10)$$

$$n_e(x, y, \lambda) = n_b(\lambda) + \Delta n_{PE} C(x, y) \quad (3.11)$$

where  $b$  is a parameter associated with the shape of the profile,  $d_x$  and  $d_y$  are the effective depth in the vertical  $x$  and horizontal  $y$  direction, respectively as indicated in Figure 3.10 (b). These parameters can be

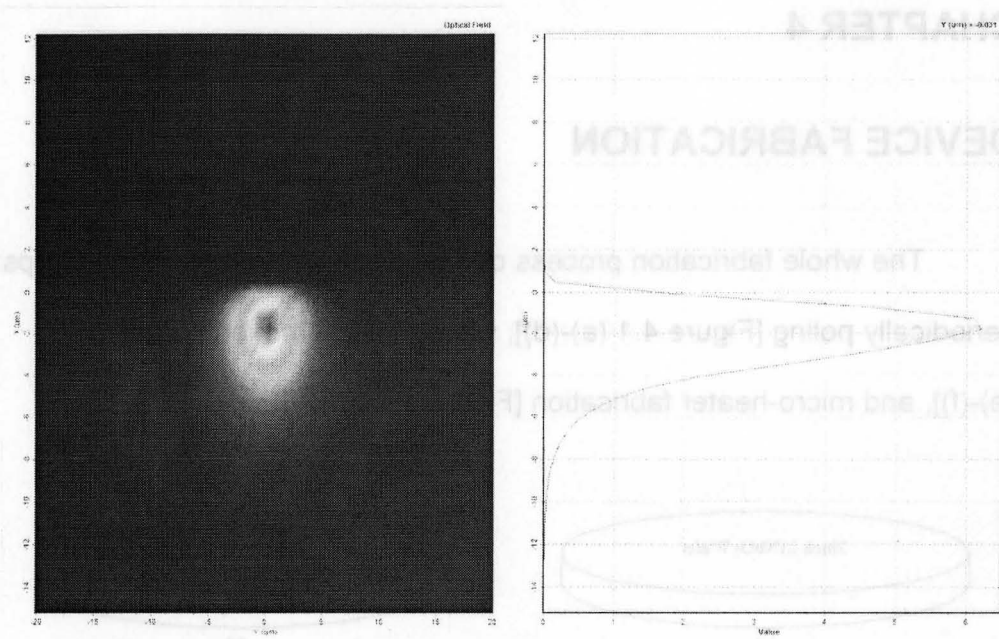
reached by fitting the theoretical results with the experimental results. And  $w$  is the mask open width,  $n_b$  is the substrate refractive index,  $\Delta n_{PE}$  is the refractive index change induces by PE process.

The extraordinary refractive index distribution generated by the equation 3.10 and 3.11 is used as the input data for the commercial simulation software APSS from Apollo Photonics Inc. For the conventional APE LiNbO<sub>3</sub> waveguide simulation, the upper boundary of the waveguide is the LN-air interface. The refractive index of air is assumed as 1. The simulation result is shown in Figure 3.11 (a). We can find the light mode leaks into the air about 1.5  $\mu\text{m}$  deep, which means we need a buffer layer thicker than 1.5  $\mu\text{m}$ .

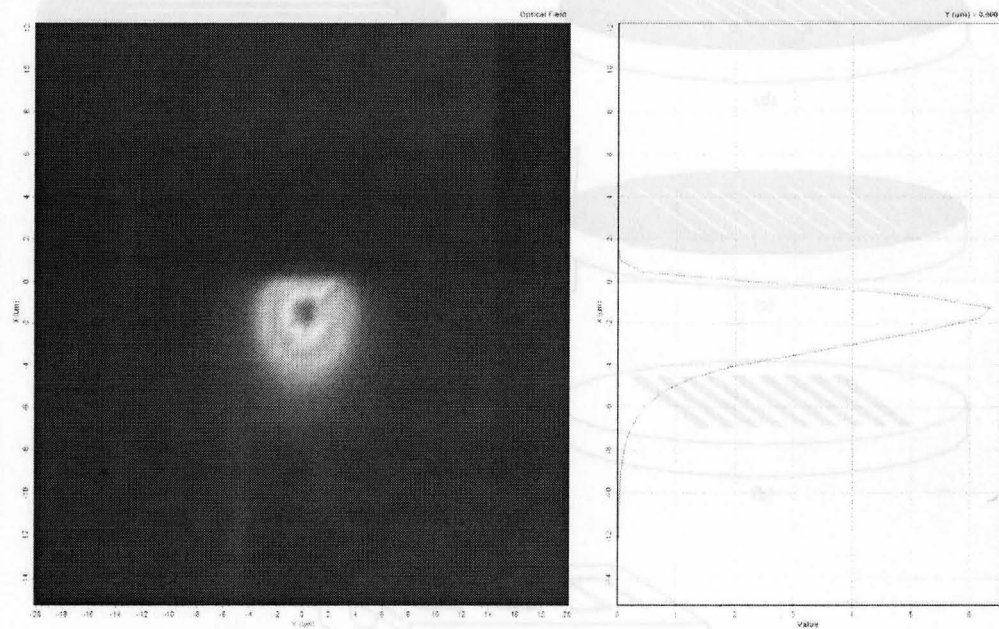
Silicon oxide is a good choice for the buffer layer because of its simple deposition process and good thermal conductivity. But it is hard to deposit a silicon oxide layer with the thickness of several micro meters. We have deposited a silicon oxide film on the LiNbO<sub>3</sub> wafer at first. SiH<sub>4</sub> and N<sub>2</sub>O are mixed (90:70) in a vacuum chamber (650 mTorr) at the temperature of 300 °C. A 500 nm thick silicon oxide film is deposited in 10 minutes under 50 W power. Because the limitation of the equipment, we can only achieved 500 nm thick film. When we input the light into the waveguide that covered by this silicon oxide buffer layer and the micro-heater layer, the output light is zero. All the light energy are absobed by the metal layer. If we input the light into the waveguides which are not

under the metal layer, nearly all light can pass through the waveguide (waveguide loss less than 0.1 dB) despite the coupling loss. In this case, we have to focus on the polymer materials which can achieve thicker film. SU-8 photoresist becomes next candidate.

Then for our integrated micro heater design, the surface of  $\text{LiNbO}_3$  is covered by a SU-8 polymer layer. The upper boundary is the LN-polymer interface. The refractive index of SU-8 photoresist is about 1.8. Using the same simulator, we can get the light mode results as shown in Figure 3.11 (b). From the simulation result, we can see that the effect of the polymer buffer layer is almost negligible. The light mode leaks into the polymer layer about  $1.5 \mu\text{m}$  deep, almost the same as the structure without buffer layer. So, the thickness of the buffer layer has to be larger than this value to ensure the light will not leak into the outside metal layers when propagating along the waveguide.



(a)



(b)

**Figure 3.11 Fundamental TM mode profile for APE LiNbO<sub>3</sub> waveguide (a) and APE LiNbO<sub>3</sub> waveguide with a polymer buffer layer (b)**

## CHAPTER 4

### DEVICE FABRICATION

The whole fabrication process can be divided into three major steps: periodically poling [Figure 4.1 (a)-(d)], waveguide formation [Figure 4.1 (e)-(f)], and micro-heater fabrication [Figure 4.1 (g)-(h)].

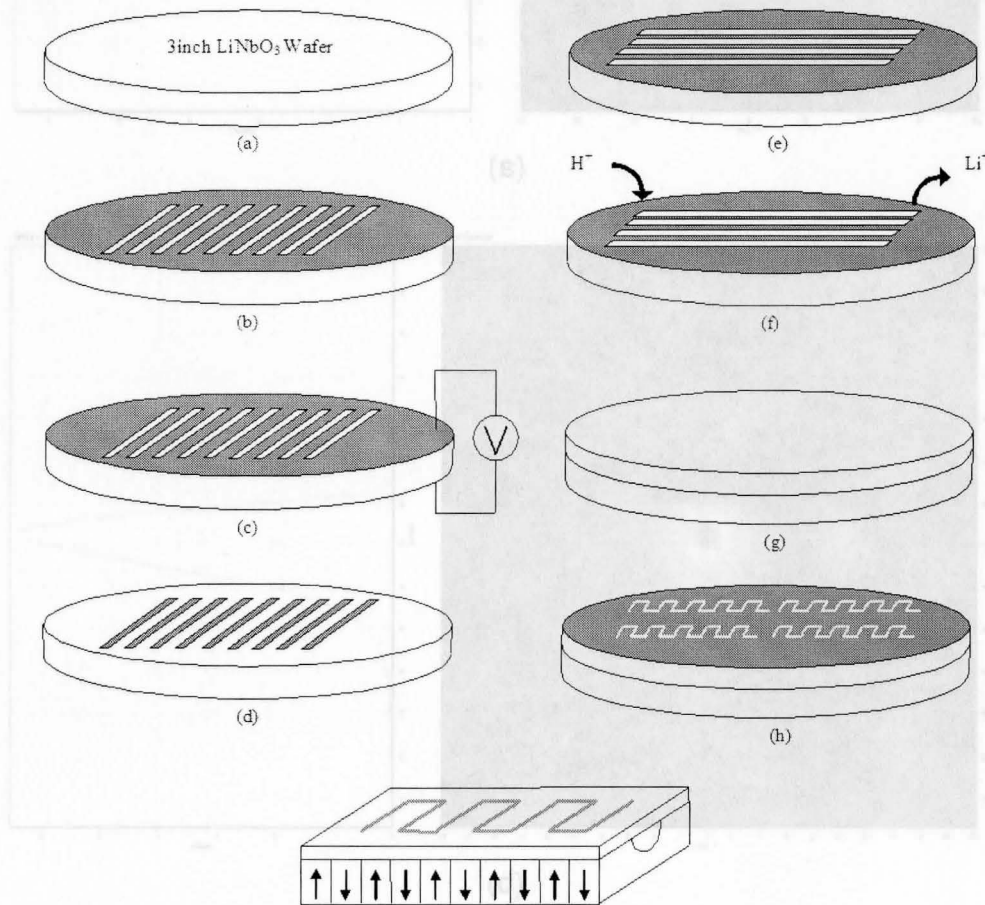


Figure 4.1 Fabrication Process for PPLN with integrated micro-heater

## 4.1 Fabrication of QPM Gratings

Although crystal manufacturers have reached a state to easily provide  $\text{LiNbO}_3$  wafers in 125 mm diameter, considering the cost and fabrication difficulty, 3-inch and 4-inch wafers are commonly used for optoelectronic guided-wave devices. In this project, our fabrication process begins with a z-cut 3 inch  $\text{LiNbO}_3$  wafer [Figure 4.1 (a)].

Since the idea of QPM was first proposed in the 1960's [37], several different approaches have been developed for the fabrication of periodic domain inversion structure in  $\text{LiNbO}_3$  and other possible materials. These fabrication methods include the modulation of the heat input during laser-heated pedestal growth, direct writing using an electron beam, and titanium indiffusion. Progress in this field was reviewed by Byer in 1997 [39]. More recently, the most practical approach was originated with Yamada et al. in 1993. He used a static electric field to invert the orientation of the ferroelectric domains in a thin crystal wafer [51]. This method is usually called electric-poling technique.

When an electric field, which is higher than the characteristic coercive field, is applied to a thin  $\text{LiNbO}_3$  crystal wafer, the orientation of the spontaneous polarization is reversed. This leads to the sign reversal of the nonlinear optical coefficients. Then by defining a periodic electric field through some methods, we can achieve a periodic domain inversion structure in the  $\text{LiNbO}_3$  crystal to satisfy the requirement of the QPM

condition. As shown in Figure 4.1 (b), after the necessary cleaning processes have been carried out, the +z surface of a z-cut  $\text{LiNbO}_3$  wafer was patterned with photoresist to define the poling electrodes through the standard lithographic processing. The linewidth of the electrode patterns are usually narrower than the QPM grating period, because the rest of the process will shrink the photoresist and expand the inversion area. After post-baking, the wafer is assembled into an apparatus shown in Figure 4.2. A high voltage is applied across the  $\text{LiNbO}_3$  wafer from  $-z$  face to  $+z$  face by using a liquid electrode (saturated aqueous solution of  $\text{LiCl}$ ). Typically, the voltage is around 21 KV. Rubber O-rings are used for electrolyte sealing. This setup is suitable for producing large-area domain-inverted gratings without the need for a vacuum or an insulator liquid.

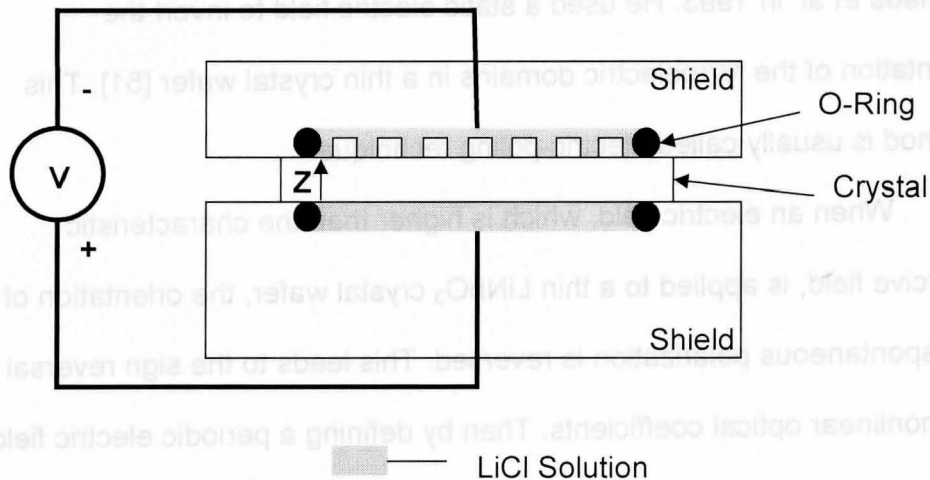
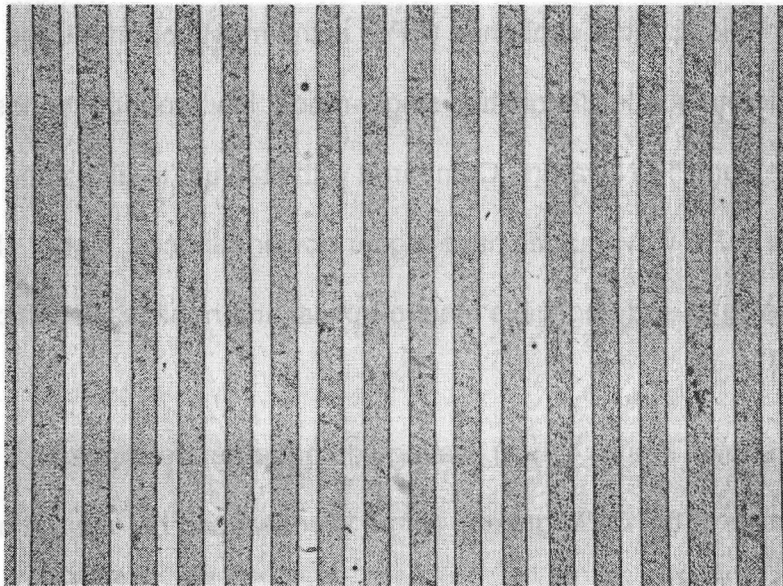


Figure 4.2 Liquid electrode poling setup

The quality of a periodically poled structure is mainly determined by two factors: periodicity and duty cycle. The periodicity of the QPM gratings strongly affects the QPM wavelength, while the duty cycle affects the conversion efficiency. Maximum conversion efficiency can be achieved for a uniform grating structure with a duty cycle of 50%. Moreover, in order to obtain high conversion efficiency, the inversion interface must be perpendicular in depth. Figure 4.3 shows a microscopic picture of a periodically poled sample with a period of  $18.7\ \mu\text{m}$ . As shown in the picture, a uniform QPM structure over a full three inch  $\text{LiNbO}_3$  wafer is achieved.



**Figure 4.3 Microscopic picture of PPLN surface**

## 4.2 Fabrication of Waveguides

After completion of the domain-inverted grating structure fabrication, the second step is to fabricate optical waveguides on the LiNbO<sub>3</sub> wafer. The waveguides are fabricated in the direction perpendicular to the QPM gratings. A number of articles on the LiNbO<sub>3</sub> optical waveguide fabrication and characterization have been published. Optical waveguides on LiNbO<sub>3</sub> can be catalogued into two types: diffused type and ridge type. Although ridge type waveguides have better light confinement than the diffused type, their fabrication techniques, such as wet etching, dry etching or wafer bonding, are not well developed yet. At this time, the most widely used fabrication techniques are titanium in-diffusion and proton exchange.

Annealed/proton-exchange (APE) is the most important and attractive technique for fabricating single-mode, low propagation loss waveguides on PPLN wafers. Compared with titanium in-diffusion waveguide, APE waveguides have higher power capacity, higher ability to confine the light, and negligible electro-optical and nonlinear coefficients decrease.

As shown Figure 4.1 (e), waveguide patterns are aligned perpendicular to the QPM grating. Stripe windows can be opened by either the etching or lift-off processes on aluminum, silicon oxide, or chromium mask layer. The thickness of the mask is ~0.1  $\mu\text{m}$ . Then the wafer with the mask is immersed in a proton source for proton-exchange

[Figure 4.1 (f)]. The molten benzoic acid is usually used at a temperature ranging from 160 to 240 °C. After several tens of minutes, the wafer is taken out. After cooling down and removal of the mask, the wafer is thermally annealed in air atmosphere for hours to reduce the propagation loss and to recover the nonlinear coefficient. The facilities for PE process and Annealing process are shown in Figure 4.4 and Figure 4.5.

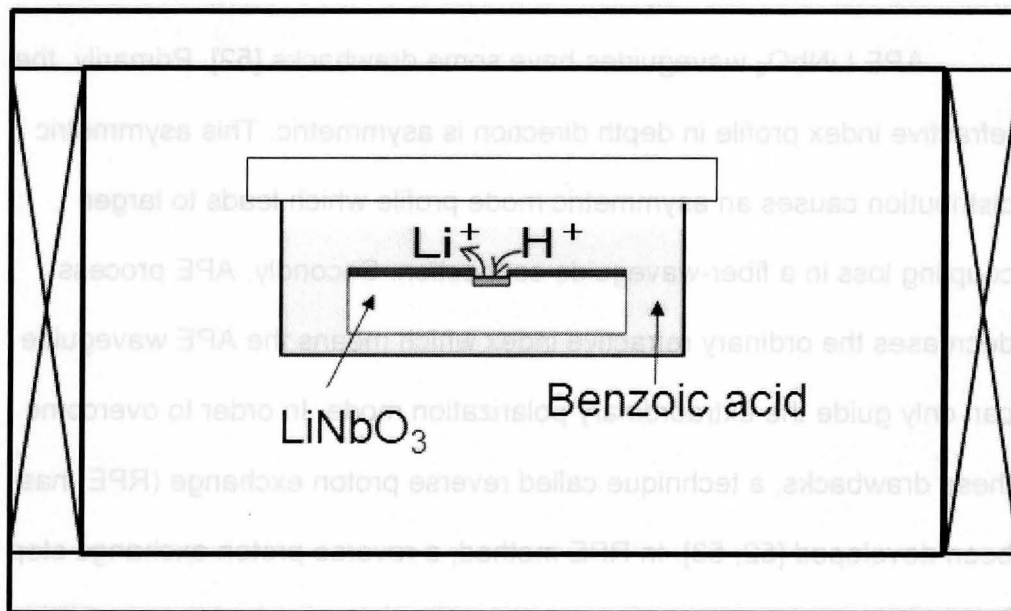


Figure 4.4 Equipment setup for proton-exchange

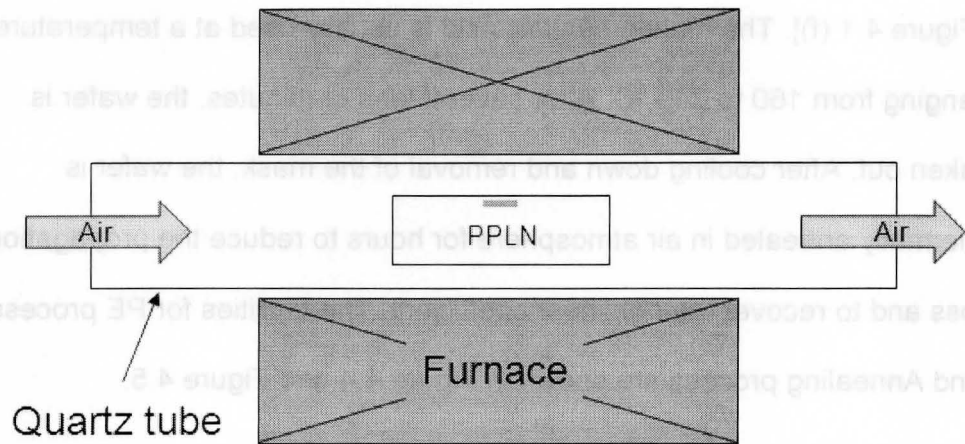
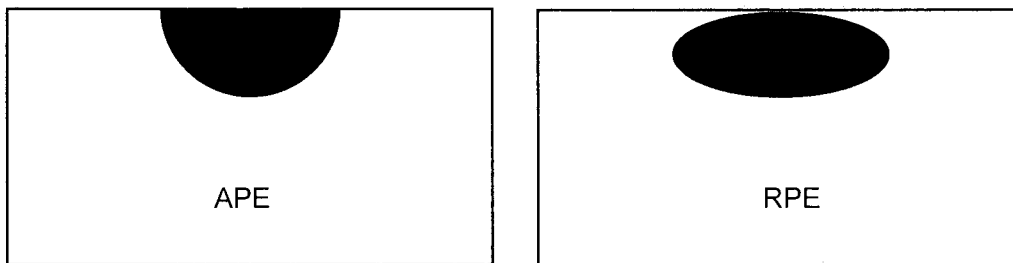


Figure 4.5 Equipment setup for annealing

APE LiNbO<sub>3</sub> waveguides have some drawbacks [52]. Primarily, the refractive index profile in depth direction is asymmetric. This asymmetric distribution causes an asymmetric mode profile which leads to larger coupling loss in a fiber-waveguide connection. Secondly, APE process decreases the ordinary refractive index which means the APE waveguide can only guide the extraordinary polarization mode. In order to overcome these drawbacks, a technique called reverse proton exchange (RPE) has been developed [52, 53]. In RPE method, a reverse proton exchange step is added after normal APE process. This RPE process exchanges the hydrogen atoms back to Li<sup>+</sup>, reduces the H<sup>+</sup> concentration in the vicinity of the surface and pushes the H<sup>+</sup> concentration maximum below the crystal surface which causes the waveguide to be buried. This process also slightly increases the ordinary refractive index, which allows for the ordinary polarization mode guiding. Figure 4.6 shows a comparison of

APE waveguides and RPE waveguides. RPE waveguides can provide symmetric shape of the waveguide modes for better fiber-waveguide coupling and better overlap between the interacting modes with different wavelength makes the conversion efficiency much higher than APE waveguide. Moreover, synchronously guiding TE and TM mode can be used for some Type-II QPM devices in certain applications.



**Figure 4.6 Comparisons of APE and RPE waveguides**

Figure 4.7 shows a typical apparatus for RPE process, the APE waveguide is immersed into a  $\text{Li}^+$  rich melt (eutectic salt of  $\text{LiNO}_3:\text{KNO}_3:\text{NaNO}_3$  with mol ratio of 37.5:44.5:18.0) at 326 °C for 90 minutes. Stirring of the eutectic salt is necessary to obtain uniform RPE waveguides.

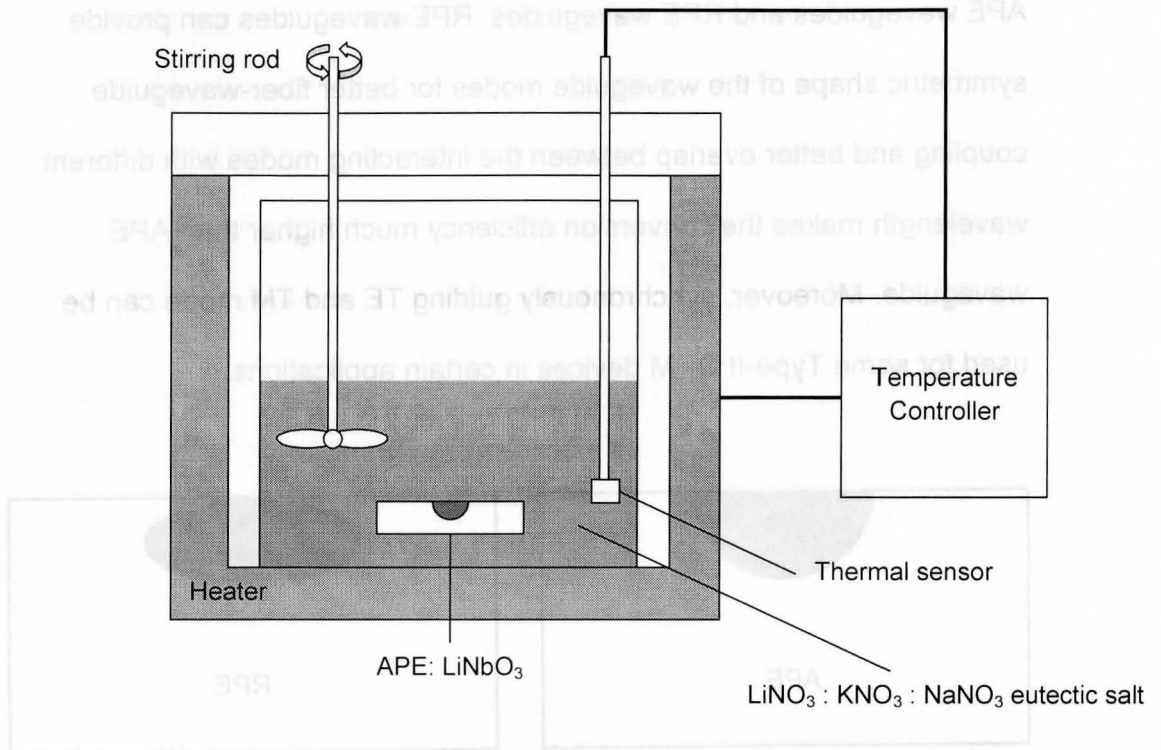
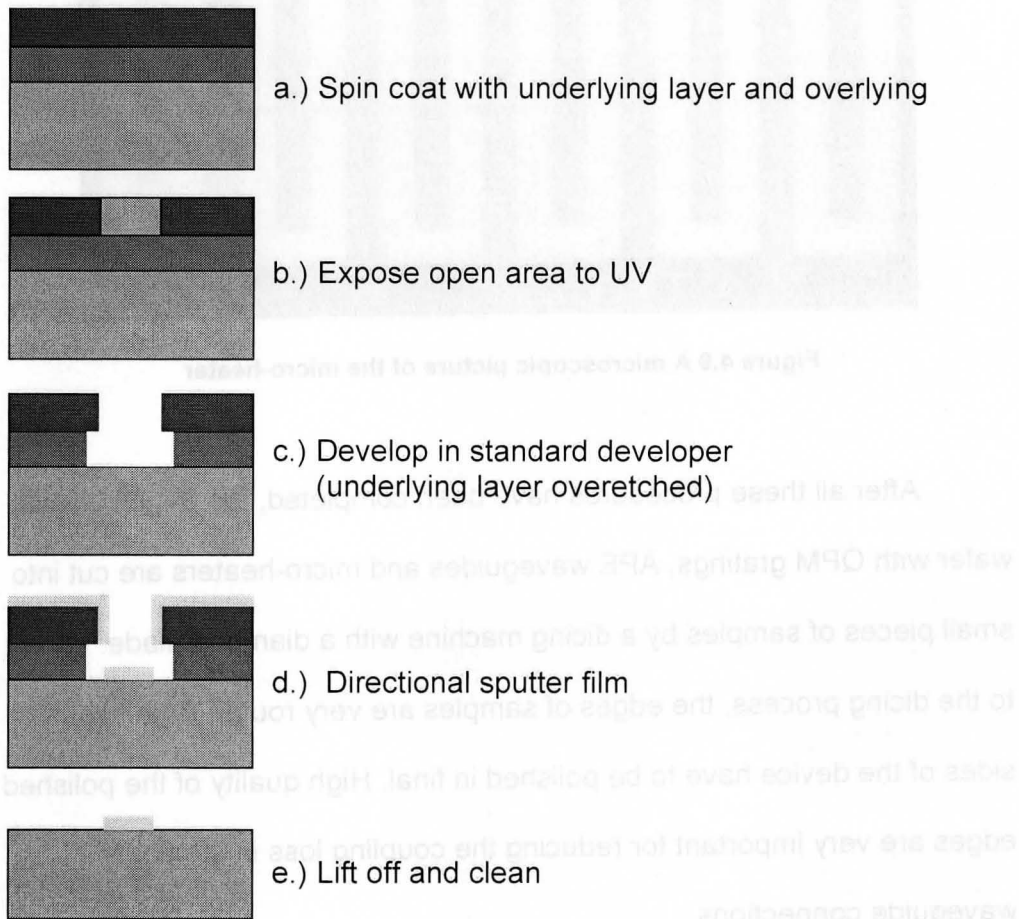


Figure 4.7 Equipment setup for RPE process

### 4.3 Buffer Layer, Micro-heater and Dicing

The third major step is the micro-heater structure fabrication. A polymer layer, around 20  $\mu\text{m}$  thick is spun on the surface to act as a buffer layer [Figure 4.1 (g)]. The polymer we used in the process is SU-8 photoresist from MicroChem Inc. The SU-8 is a negative, epoxy-type, near-UV photoresist (365 nm). The refractive index of SU-8 is about 1.7 to 1.8. The film thickness is highly dependent on the spin speed. In our case, a 20  $\mu\text{m}$  thick film layer is achieved at the spin speed of 2,500 rpm. Since

there is no structure for this buffer layer, the wafer with SU-8 photoresist is placed on a hotplate at the temperature of 200 °C for hard bake (curing).



**Figure 4.8 Lift-off process**

Then a Cr/Pt/Au multi metal layer with the thickness of 30 nm /250 nm /150 nm is deposited on the PPLN sample. The pattern of micro-heaters is fabricated by a standard lift-off process as shown in Figure 4.8. Figure 4.9 shows a microscopic picture of the micro heater electrode.

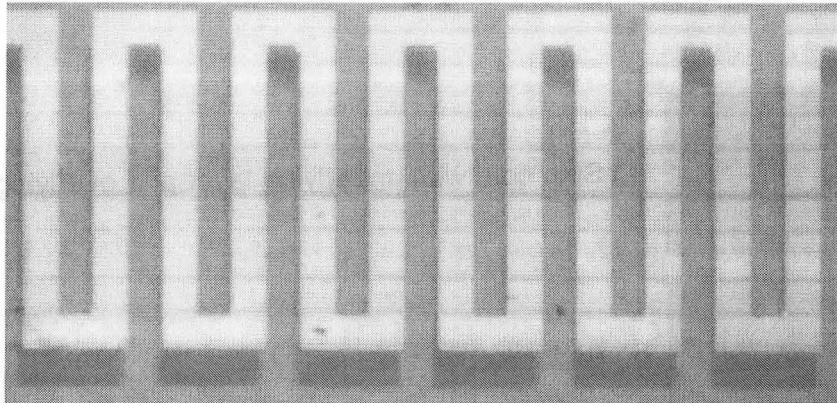


**Figure 4.9 A microscopic picture of the micro-heater**

After all these procedures have been completed, the 3-inch  $\text{LiNbO}_3$  wafer with QPM gratings, APE waveguides and micro-heaters are cut into small pieces of samples by a dicing machine with a diamond blade. Due to the dicing process, the edges of samples are very rough. Both two sides of the device have to be polished in final. High quality of the polished edges are very important for reducing the coupling loss in the fiber-waveguide connections.

## CHAPTER 5

### EXPERIMENTS AND RESULTS DISCUSSION

#### 5.1 Wavelength Converter Packaging

Efficiently coupling the laser light into the APE LiNbO<sub>3</sub> waveguide is one of the key design issues for both experimental and practical applications. For most cases, the single mode fiber is directly aligned with the waveguide for coupling the light without any other optical components. Proper alignment is very critical and important. There are three types of misalignments that affect the coupling efficiency when a single mode fiber is aligned with a waveguide [54].

The first form of misalignment is called transverse misalignment. It refers to any possible displacement between the center axis of the fiber and the waveguide. A schematic diagram of transverse misalignment is shown in Figure 5.1. This form of misalignment can exist anywhere in the planes parallel to the plane of the fiber or waveguide facets.

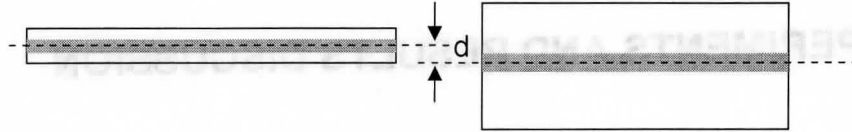


**Figure 5.1 A transverse misalignment between a fiber and a waveguide**

The power transmissivity dependence upon transverse misalignment can be given as [54]:

$$T = T_{MAX} \exp\left(-\frac{2d^2}{\omega_f^2 + \omega_s^2}\right) \quad (5.1)$$

where  $d$  is the displacement, and  $\omega_f, \omega_s$  are the spot size of a single mode SMF-28 fiber and a lithium niobate waveguide, respectively. The different kind of expressions of these two parameters can be found in many research literatures.

The second form of misalignment that may cause optical loss at a fiber-waveguide connection is longitudinal misalignment. As shown in Figure 5.2, the longitudinal misalignment describes the gap width between the fiber facet and waveguide facet.

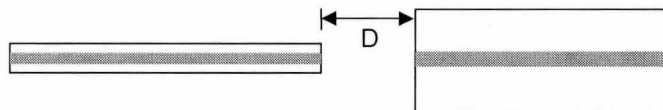


**Figure 5.2 A longitudinal misalignment between a fiber and a waveguide**

The power transmissivity sensitivity for longitudinal misalignment can be determined from the following equation [55]:

$$T = T_{MAX} \exp\left(-\left(\frac{D}{S_e}\right)^2\right) \quad (5.2)$$

$$S_e = \frac{\sqrt{2}}{2} \left(\frac{2\pi}{\lambda_0}\right) (\omega_f^2 + \omega_s^2) \quad (5.3)$$

similarly as in equation 5.1,  $\omega_f, \omega_s$  are the spot size of a single mode SMF-28 fiber and a lithium niobate waveguide, respectively.

The third important source of optical loss is called angular misalignment. Figure 5.3 shows an example of angular misalignment between a fiber and a waveguide.

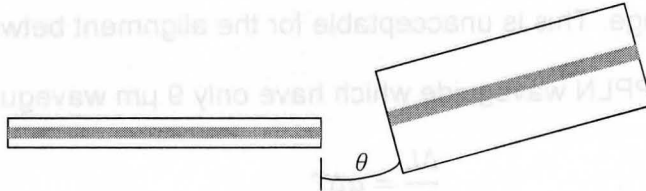


**Figure 5.3 An angular misalignment between a fiber and a waveguide**

The power transmissivity sensitivity of angular misalignment can be written in the form as [54]:

$$T(\theta) = \left(\frac{2\omega_f\omega_s}{\omega_f^2 + \omega_s^2}\right)^2 \exp\left(-\frac{\left(\frac{2\pi}{\lambda_0}\right)^2 n_l^2 \theta^2 \omega_f^2 \omega_s^2}{2(\omega_f^2 + \omega_s^2)}\right) \quad (5.4)$$

where  $n_l$  is the refractive index of the medium between the fiber and the waveguide and  $\omega_f, \omega_s$  are the spot size of a single mode SMF-28 fiber and a lithium niobate waveguide, respectively.

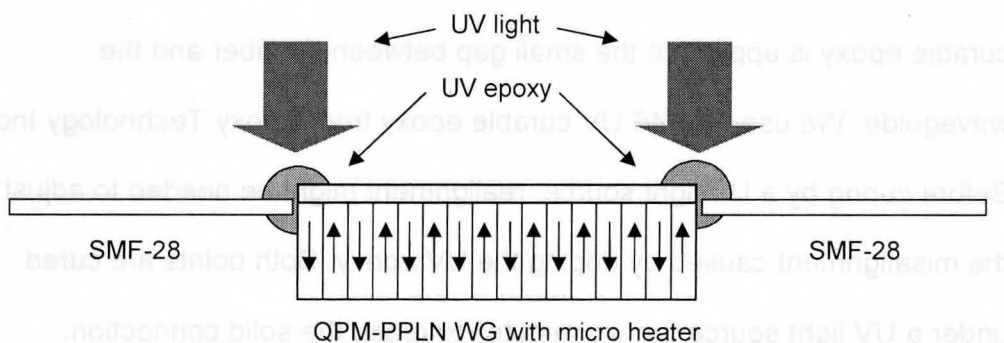
From the equations 5.1, 5.2 and 5.4, we can easily find that the power transmissivity of Fiber-waveguide coupling exponentially increases with the value of the misalignments, which means the coupling efficiency is very sensitive to the accuracy of the alignment.

In our case, the alignment issue is more critical. As a QPM-PPLN waveguide device with an integrated micro heater, the temperature device will be tuned from room temperature to over 120 °C. Using the linear thermal expansion equation 4.5, we can have calculated that the lithium niobate crystal has about 12  $\mu\text{m}$  expansion in width with over 100 °C temperature change. This is unacceptable for the alignment between a SMF-28 and the PPLN waveguide which have only 9  $\mu\text{m}$  waveguide width.

$$\frac{\Delta L}{L_0} = \alpha \Delta T \quad (5.5)$$

As a result, using a proper packaging method to fix the relative position between the fiber and the waveguide is necessary for the following experiments. The simplest way is using UV curable epoxy to attach the fiber with the waveguide. The UV curable epoxy has several advantages. The first is that the UV curable epoxy can be cured by UV light at room temperature in less than 2 minutes while the normal heat epoxies require the device be placed in a high temperature for tens of

minutes. This advantage can minimize the possible misalignments and induced stress during the curing process. Moreover, the UV curable epoxy that we use for package has a refractive index of about 1.5 at the wavelength around 1550 nm. This value is between the refractive index of the fiber and lithium niobate waveguide which can reduce back reflection at any of these facets.



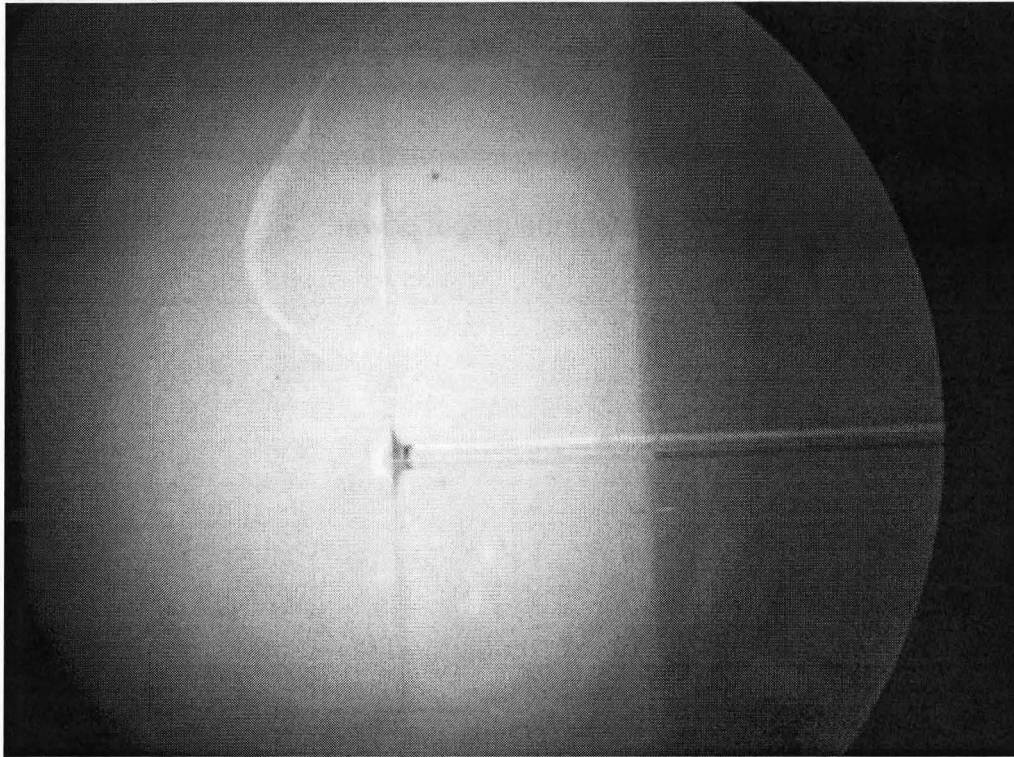
**Figure 5.4 The fiber-to-waveguide connected by UV curable epoxy**

Figure 5.4 shows the experimental process for connecting the single mode fiber to the QPM-PPLN waveguide by UV curable epoxy. Both input and output fibers are aligned to the device using the 3-axis alignment stages. At first, with the assistance of a microscope, the input single mode fiber and an output multi mode fiber are manually aligned to the waveguide. The multi mode fiber used here is for more easily catching the light. Then the input fiber is connected to the light source and the

output fiber is connected to the power meter. A coarse alignment is initially operated manually to detect the light signal. Once a signal power on the mW scale is detected by the power meter, the light is successfully being coupled into the waveguide. Then the output multi mode fiber is changed to another single mode one. After this, we used a piezoelectric controller to precisely align the input and output fibers till reaching the maximum power at the power meter.

After the alignment of the input and output fibers to the device, UV curable epoxy is applied to the small gap between the fiber and the waveguide. We use OG146 UV curable epoxy from Epoxy Technology Inc. Before curing by a UV light source, realignment might be needed to adjust the misalignment caused by doping the UV epoxy. Both points are cured under a UV light source for two minutes to reach the solid connection.

Figure 5.5 shows the fiber-waveguide joint after UV curing under a microscope. This joint is very delicate and sensitive to any mechanical stress, since the cross-sectional area is so small. If more mechanical durability is required for applications, it would be worthwhile to cure the input and output fibers to the same surface that the lithium niobate substrate is attached to and using some components to raise the fibers to be the same height as the waveguide.



**Figure 5.5 A UV epoxy fiber-waveguide connection joint**

In order to validate that this simple package is effective for reducing the misalignment caused by thermal expansion effect, we use an external bulk oven to change the temperature of the device while a certain power of light goes through the device. By monitoring the power change, we can verify if there is any coupling loss change. The schematic diagram of this experimental setup is shown in Figure 5.6. We use a tunable laser (HP, model: 81640A) as the light source. After being amplified by an erbium doped fiber amplifier (EDFA) (Oprel, model: OFA20D-2211S), the laser light is inputted into the fiber and goes through the device. The output fiber

is connected to a power meter to measure the output power. The wavelength of the tunable laser is set to a wavelength that is a little bit far from the device's QPM wavelength to eliminate any possible nonlinear interactions which might be effect the output power.

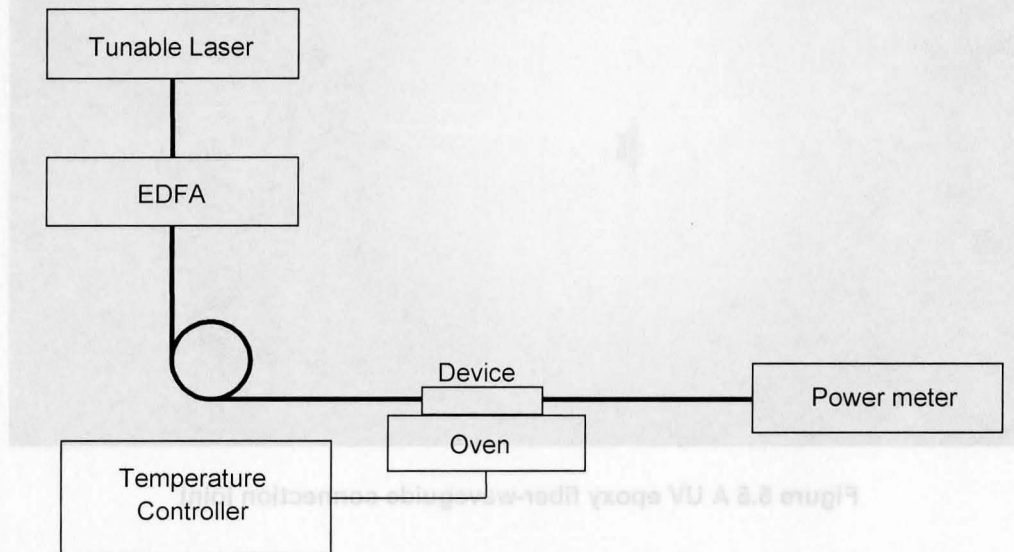


Figure 5.6 Experimental setup for the fiber-waveguide connection package

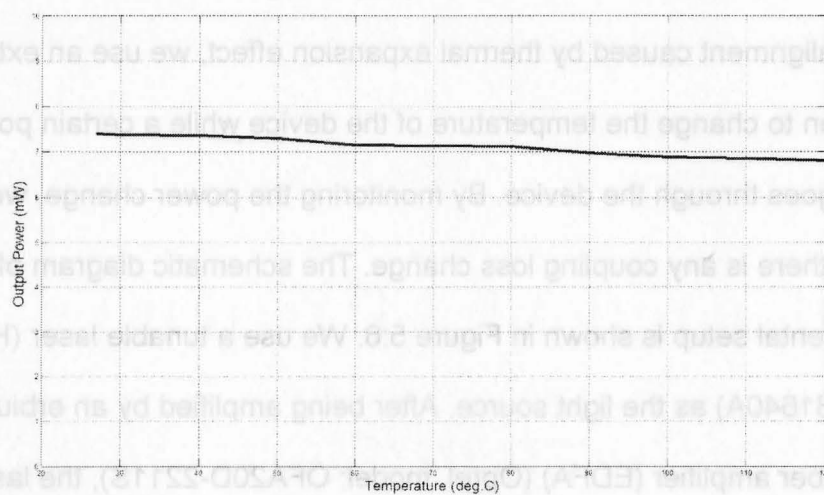
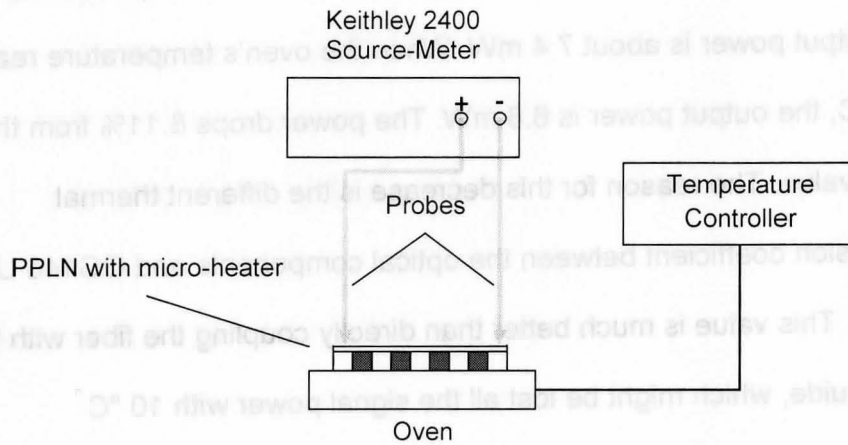


Figure 5.7 Output Power dependence upon Temperature

The test result is shown in Figure 5.7. At room temperature (27 °C), the output power is about 7.4 mW. When the oven's temperature reaches 120 °C, the output power is 6.8 mW. The power drops 8.11% from the initial value. The reason for this decrease is the different thermal expansion coefficient between the optical components and OG146 UV epoxy. This value is much better than directly coupling the fiber with the waveguide, which might be lost all the signal power with 10 °C temperature change. Especially for our wavelength tuning experiments, this value is acceptable because we are more concerned more about the wavelength shift rather than the power change.

## **5.2 Electrical characterization**

Before investigating the optical properties of the device, some electrical characterization of the micro-heater are necessary. The electrical characterization setup is very simple as shown in the Figure 5.8. The device is placed on an external oven (Thorlabs, model PV40), which is connected to a temperature controller (Thorlabs, model TC200). Two micro-probes are used for the connection between the micro-heater and a source-meter (Keithley, model 2400), which can work for current supplying and voltage or resistance measurement at the same time.



**Figure 5.8 Electrical characterization setup**

One of the interesting features of this integrated multi-layer metal micro-heater design is that the metal layer can also act as a temperature sensor while it is working as the micro-heater. That is because the resistivity of metal materials is strongly temperature dependent. At high temperatures, the resistance of a metal increases linearly with temperature. As the temperature of a metal is reduced, the temperature dependence of resistivity follows a power law function of temperature. Therefore, in the temperature range that our device works for, the resistance of the micro-heater linearly increases with temperature which can be simply written as:

$$R = R_0 + \alpha\Delta T \quad (5.6)$$

where  $R_0$  is the initial resistance,  $\alpha$  is the temperature coefficient, and  $\Delta T$  is the temperature change.

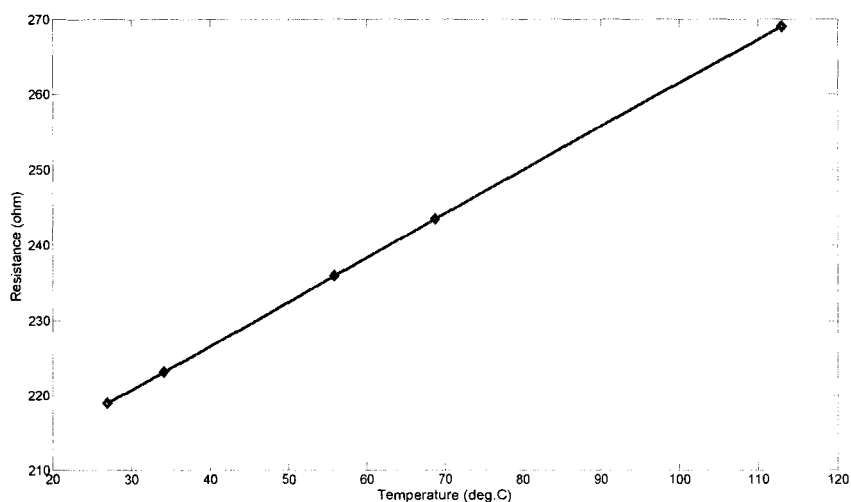


**Figure 5.9 Micro-heater Resistance versus Temperature**

At room temperature (27 °C), we measure that the resistance of the micro-heater is 218.7  $\Omega$ . This value is bigger than the value that we calculated in the Chapter 3 because of some of the alloy effects between different metal layers during the fabrication process. To validate the relationship of equation 5.6 and find out the temperature coefficient of the micro-heater, the device is heated from room temperature to 120 °C by the oven, while the resistance is being measured at the same time by the 2400 source-meter. Then we get the temperature dependence of the micro-heater's resistance as shown in Figure 5.9. The temperature coefficient can be simply calculated as 0.558  $\Omega/^\circ\text{C}$ .

Then by using the source-meter, we can measure the resistance while applying the working current. The resistance can indicate the

temperature of the micro-heater when it is working at certain injected current.

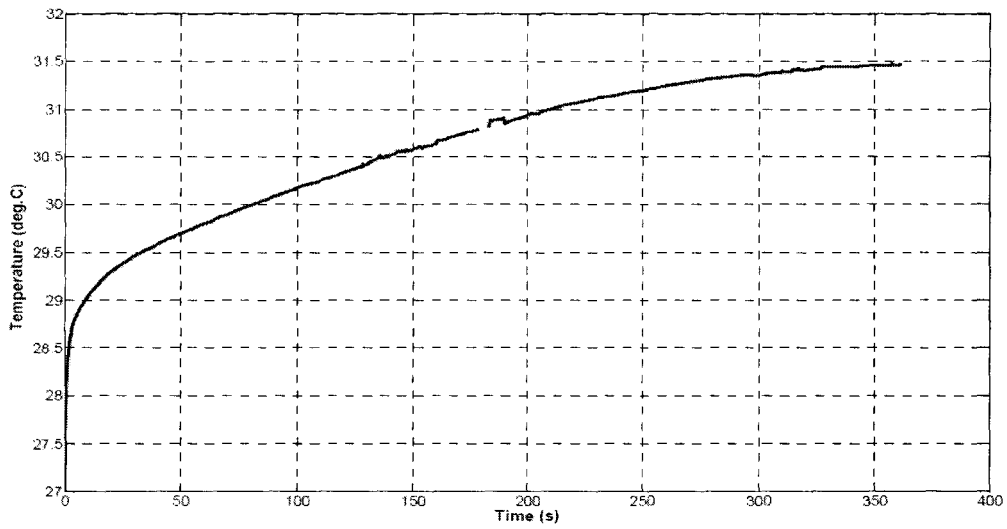


**Figure 5.10 Temperature change with 25 mA injection current**

Figure 5.10 shows the temperature curve when 25 mA current is applied. We can see that 25 mA injection current makes the device heated to 31.5 °C. The temperature is suddenly raised in the first 10 to 20 seconds and then tends to reach the 31.5 °C.

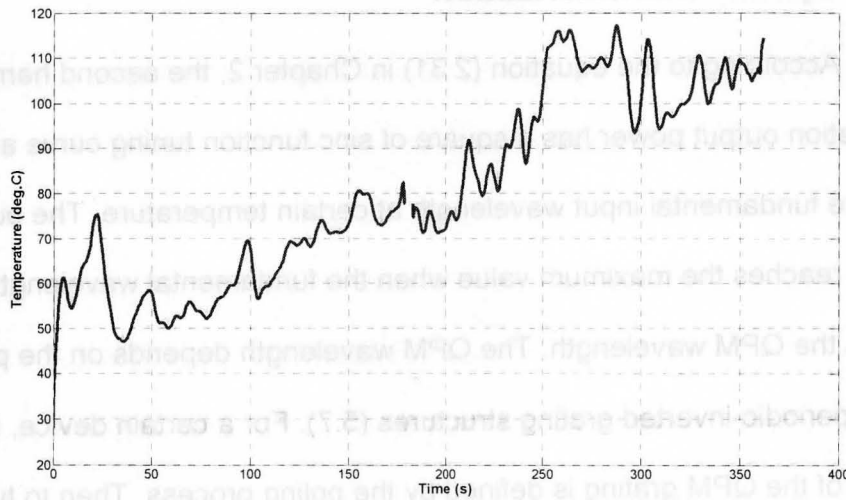


**Figure 5.11 Temperature change with 125 mA injection current**

When injecting 125 mA current into the micro-heater, the device temperature eventually reaches about 120 °C. The curve is rougher than at low current because that high temperature aggravates the heat exchange between the device and around components or air, which might causes the unstable of temperature distribution in the device.



**Figure 8.15 A schematic diagram of temperature tuning process**

### 5.3 Optical characterization

According to the equation (2.31) in Chapter 2, the second harmonic generation output power has a square of sinc function tuning curve along with the fundamental input wavelength at certain temperature. The output power reaches the maximum value when the fundamental wavelength equals the QPM wavelength. The QPM wavelength depends on the period of the periodic-inverted grating structures (5.7). For a certain device, the period of the QPM grating is defined by the poling process. Then to tune the QPM wavelength, we need to change the temperature of the device which leads the change of refractive index based on Sellmeier equation 2.41. A schematic diagram of this process is shown in the Figure 5.12. The SHG tuning curve shifts towards to the long wavelength while the temperature is increased from low to high.

$$\lambda = 2\Lambda(n_{2\omega} - n_{\omega}) \quad (5.7)$$

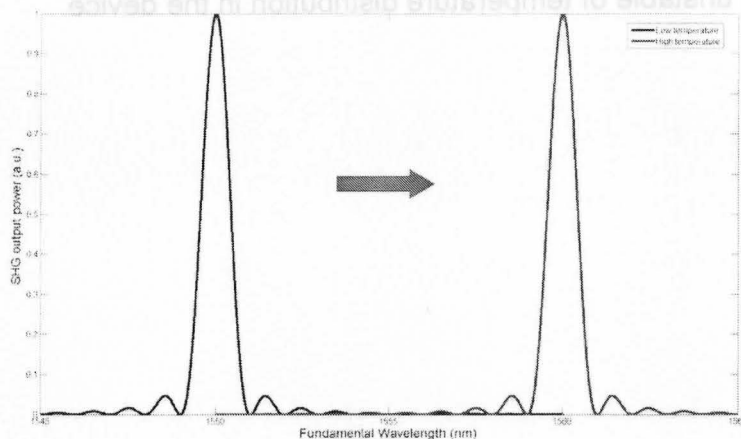
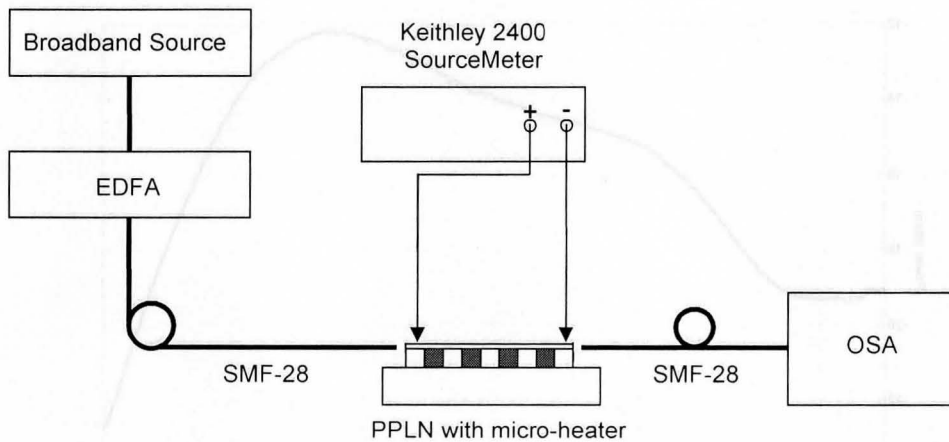


Figure 5.12 A schematic diagram of temperature tuning process

To test the tunability of our MicroHeater-integrated PPLN waveguide device, we build an experimental setup as shown in Figure 5.13.



**Figure 5.13 Experimental setup for wavelength tuning range test**

Instead of using a tunable laser, we choose a broadband light source. We found that the tunable laser output power sometimes drifted back and forth due to the variety of the tunable laser's polarization. Moreover, since the broadband source can simultaneously output light with a wide and continuous wavelength range, we can directly observe the QPM tuning curve on OSA by instead of waiting for the tunable laser to scan for minutes. The broadband source (JDSU, model: BBS1550+1 FA) can provide 20 mW light with the wavelength around 1550. The EDFA is used to amplify the fundamental light. Since the SHG output power is

proportional to the square of input fundamental power, high input power can enhance the signal-to-noise ratio (SNR). Figure 5.14 shows the amplified spontaneous emission (ASE) output spectrum from the EDFA.

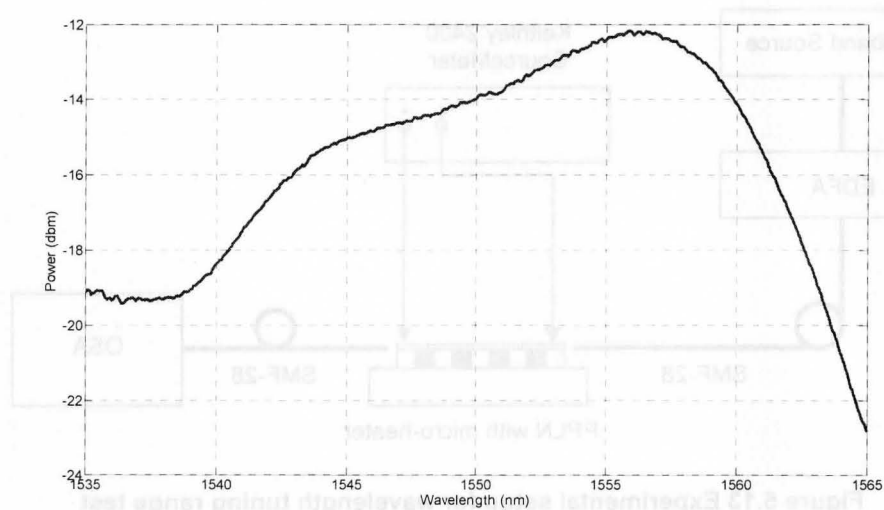


**Figure 5.14 Broadband source + EDFA output spectrum**

The simple package that was mentioned in the first section is connected to the output of EDFA. The amplified fundamental light passes through the QPM-PPLN waveguide. The output single mode fiber is connected to an optical spectrum analyzer (ANDO, model: AQ6315A). The resolution of OSA is set at 0.1 nm. The device is placed on a heat insulated holder (made by Teflon). As the same of electrical characterization setup, two micro-probes are used for connection between

the micro-heater and the source-meter. Figure 5.15 and 5.16 show the pictures of the device holder and the equipments used in the experiment.

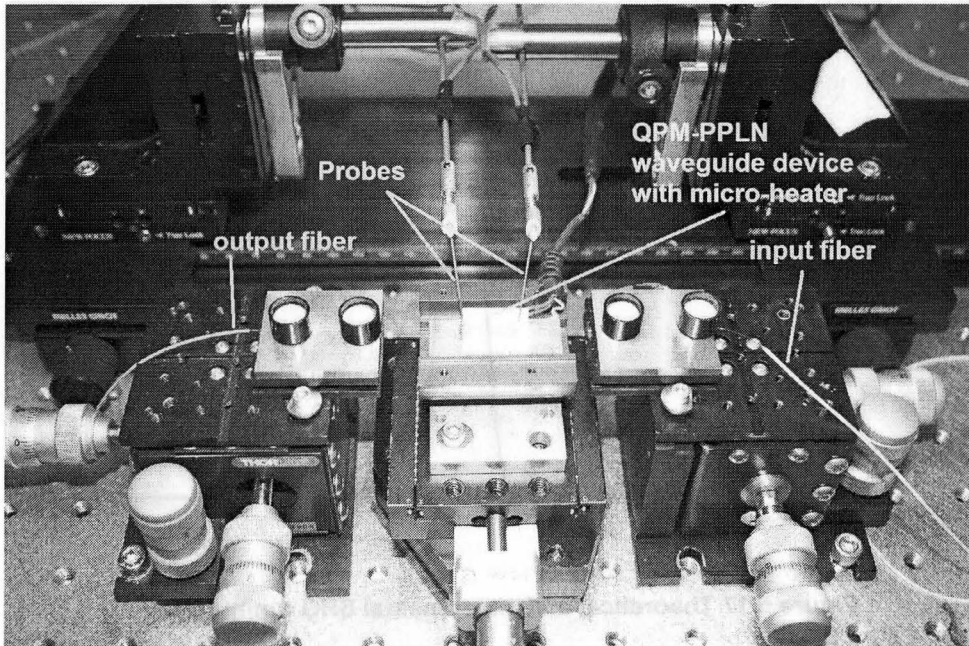


Figure 5.15 Alignment apparatus of the QPM-PPLN with integrated micro heater

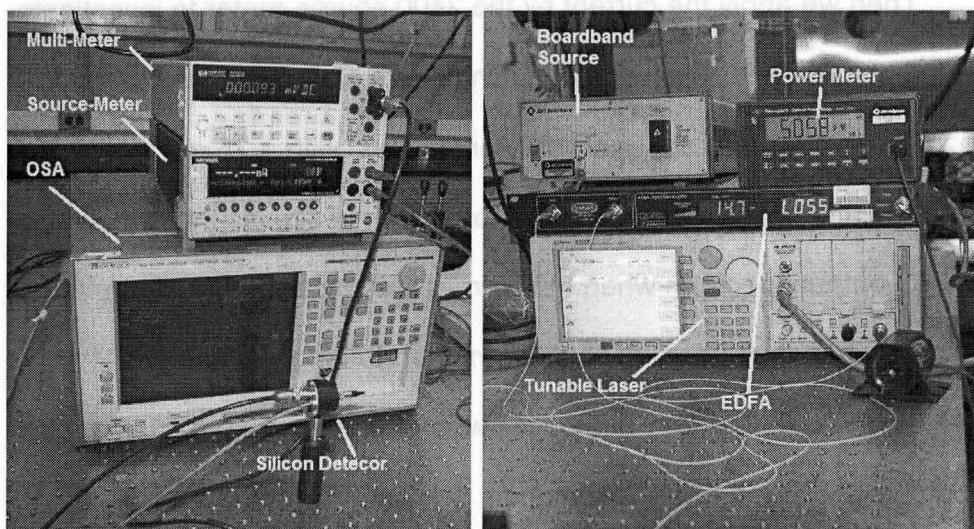
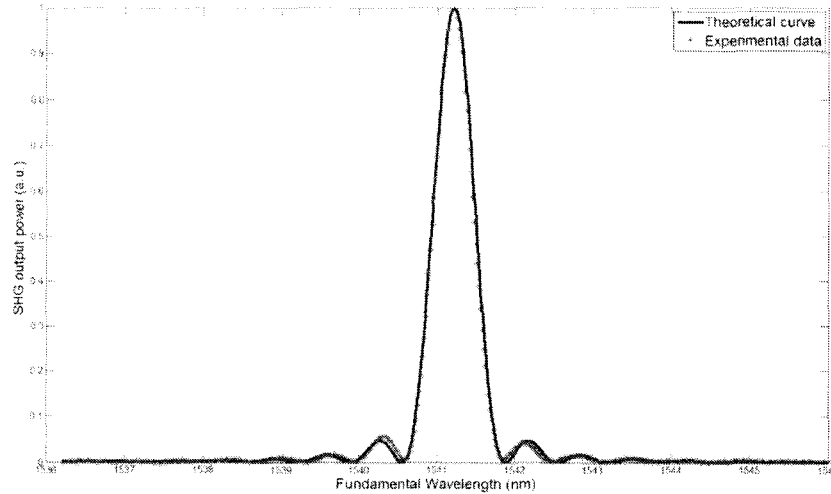


Figure 5.16 Additional equipments used for test

At room temperature, we have achieved the SHG output spectrum curve which is almost perfect match the theoretical curve (Figure 5.17).



**Figure 5.17 Theoretical and experimental SHG tuning curve**

Then we apply the current by the 2400 source-meter to investigate the shift of QPM-PPLN waveguide tuning curve along with the current. The injection current is set to six different values, with a 25 mA increased at each point. Then from the OSA, we observe the significant “red shift” of the SHG output spectrum when the current is increased. The shape stays the same when the spectrum shifts from short to long wavelength. However, the output power decreases when the temperature is high. Two reasons might cause this phenomenon. The first is that the increased temperature causes the thermal expansion of the device and the increase of refractive index, which equivalently increase the cross section area of

the waveguide. As shown in equation 2.31, the SHG output power is inversely proportional to the cross section area, thus the increase of temperature causes the decrease of SHG output power. The increase of the cross section area of the waveguide might also cause the change of the propagation mode of the fundamental light or generated light. Mode change leads to the change of the overlap of two beams which also affects the conversion efficiency. The second reason is that, as we discussed in the first section of this chapter, the input power decreases while the temperature is increasing because of the misalignment in the fiber-waveguide connections. This factor also decreases the conversion efficiency through the relationship shown in equation 2.32. Both factors cause the decrease of the SHG output power we have observed in Figure 5.18.

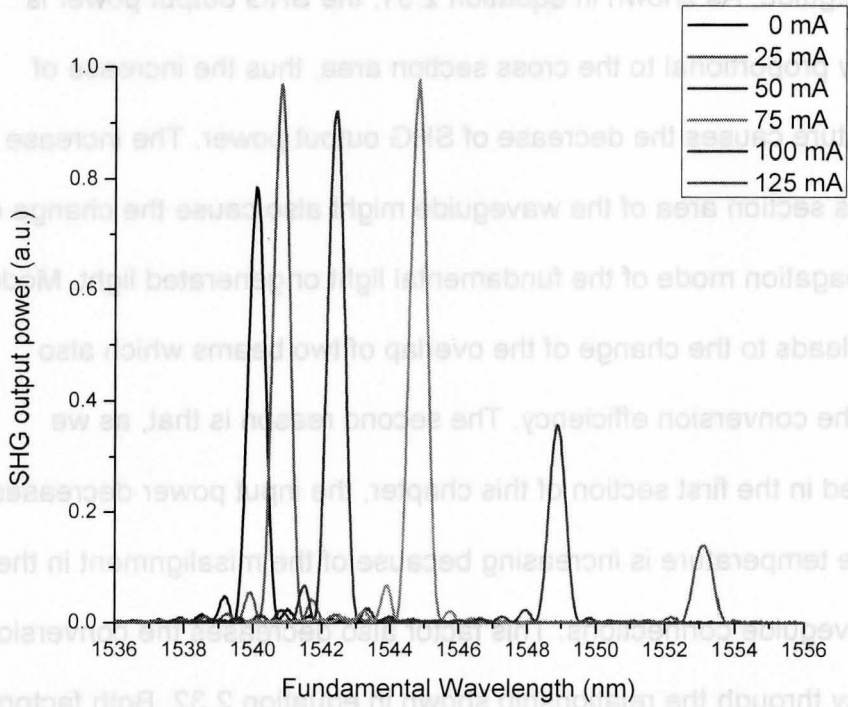


Figure 5.18 SHG output spectrums under different injection currents

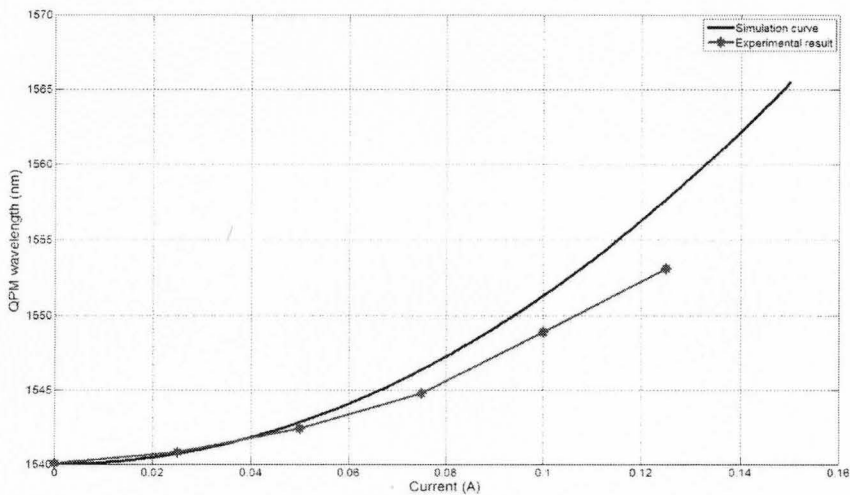


Figure 5.19 QPM wavelength versus injection current

Based on the results shown in Figure 5.18, we can draw a relationship between the QPM wavelength and the injected current (Figure 5.19). The stars and the red solid line represent experimental data and the fitting curve, respectively. The blue solid line is the theoretical simulation curve based on the discussion in the Chapter 3. We can see that with 125mA current applied, the QPM wavelength is tuned about 13 nm. As we mentioned in the last section, with 125 mA injection current, the device temperature is about 120 °C, the temperature sensitivity of the QPM wavelength for PPLN waveguide devices is about 0.138 nm/°C which matches the linear relationship between the wavelength shift and the temperature shown in Figure 2.8 (b). To achieve this temperature, only ~3 watts electric power consumption is required, which is significantly less than the power consumption of the conventional external temperature control system (nearly 20 watts). The simulation value is larger than the experimental results, especially in high injected current, because in the thermal simulation mode, we assume that the heat exchange between the device and the environment is zero. Since our device is placed in an open environment rather than in a small sealed package, high temperature aggravates the heat exchange between the device and environment, which cannot be ignored when temperature is high.

## CHAPTER 6

### CONCLUSION

#### 6.1 Summary of Research Achievements

In this thesis, a novel integrated design for tuning the wavelength of second harmonic generation in a PPLN waveguide device has been demonstrated. Device design, fabrication and performances have been studied both theoretically and experimentally

A Cr/Pt/Au multilayer metal thin film is deposited on a conventional QPM-PPLN wavelength converter with a polymer buffer layer to work as a micro-heater. When applying current to the micro-heater, the temperature in the micro-heater area is tuned, and thus the effective period of the QPM waveguide device changed due to the temperature dependence of the refractive index of PPLN, which leads to the change of QPM wavelength. In the meantime, by monitoring the resistance of the micro-heater, the temperature can be precisely measured.

The QPM wavelength can be tuned from 1540.1 nm to 1553.12 nm by applying the DC current from 0 to 125 mA. The temperature sensitivity of the QPM wavelength for PPLN waveguide devices is about 0.138 nm/°C. The power consumption is reduced to 15% as compared with the conventional external temperature control system. This design can be

widely used in all applications of PPLN devices which need temperature control or tuning.

## **6.2 Suggestions for Future Work**

Besides the achievements mentioned in this thesis, there are still many improvements that should be done in future.

The thermal distribution in the device should be analysed in detail. More accurate thermal mode can help to further optimize the design of the micro-heater to achieve lower power consumption and fast tuning speed.

The device should be optimized to achieve high and uniform conversion efficiency over the entire temperature range. A Ridge waveguide structure might be a better solution.

Potential application in Mid-IR light generation by DFG should be studied. In the DFG process, the same temperature change leads to much larger wavelength tuning. This integration design may help to build compact tunable Mid-IR light sources.

## BIBLIOGRAPHY

- [1] Y. Suzuki, H. Toba, "Recent Research and Development of All-Optical Wavelength Conversion Devices," *NTT Technical Review*, vol. 1, p 26-31, 2003.
- [2] William P. Risk, Timothy R. Gosnell, Arto V. Nurmikko, *Compact Blue-Green Lasers*, Cambridge University Press, 2003.
- [3] C.Q. Xu, K. Takemasa, K. Nakamura, H. Okayama, T. Kamijoh, "Semiconductor quasiphase matched wavelength converters," *Pacific Rim Conference on Lasers and Electro-Optics, CLEO*, p 229-230, 1997.
- [4] C.Q. Xu, "Communication applications of PPLN based all-optical wavelength converters: Advantages and challenges," *Pacific Rim Conference on Lasers and Electro-Optics, CLEO*, p 1769-1770, 2005.
- [5] J. Diao, P.L. Chu, "An all-fiber optical wavelength converter," *Proceedings of the SPIE*, vol. 3491, p 15-17, 1998.
- [6] Seung Koo Park, Jung Yun Do, Jung Jin Ju, S. Park, Min-su Kim, Myung-Hyun Lee, "Nonlinear optical polymer applicable for all-optical wavelength converters in communications bands near 1.5  $\mu\text{m}$ ," *Materials Letters*, vol. 59, p 2872-5, 2005
- [7] D. Campi, C. Coriasso, "Wavelength conversion technologies," *Photonic Network Communications*, vol. 2, p 85-95, 2000.

- [8] M.H. Chou, K.R. Parameswaran, M.M. Fejer, I. Brener, "Three-wave mixing devices for WDM applications," *LEOS Summer Topical Meeting*, p 19-21, 1999.
- [9] S.H. Wang, Lixin Xu, P.K.A. Wai, H.Y. Tam, "All-optical wavelength conversion using multi-pump Raman-assisted four-wave mixing," *Optical Fiber Communication Conference National Fiber Optic Engineers Conference*, p 330-32, 2007.
- [10] M.B. Raschke, M. Hayashi, S.H. Lin, Y.R. Shen, "Doubly-resonant sum-frequency generation spectroscopy for surface studies," *Chemical Physics Letters*, vol. 359, p 367-72, 2002.
- [11] Ming-Hsien Chou, K.R. Parameswaran, M.M. Fejer, I. Brener, "Optical signal processing and switching with second-order nonlinearities in waveguides," *IEICE Transactions on Electronics*, vol. E83-C, p 869-74, 2000.
- [12] H. Ishizuki, M. Fujimura, T. Suhara, H. Nishihara, "LiNbO<sub>3</sub> waveguide quasi-phase-matched sum-frequency generation device for high-efficiency optical sampling," *Electronics and Communications in Japan*, vol. 84, p 29-36, 2001
- [13] L. Torner, G.I. Stegeman, "Soliton evolution in quasi-phase-matched second-harmonic generation," *Journal of the Optical Society of America B*, vol. 14, p 3127-33, 1997.
- [14] L. Han, Y. Wang, W. Liang, C.Q. Xu, "Portable mid-IR source

- around 3.7  $\mu\text{m}$  based on temperature-tuned periodically poled lithium niobate (PPLN),” *Photonics North 2007, Proceedings of SPIE*, vol. 6796, p 67962J, 2008.
- [15] K.E. Stukjaer, C. Joergensen, S.L. Danielsen, B. Mikkelsen, M. Vaa, R.J. Pedersen, H. Povlsen, M. Schilling, K. Daub, K. Dutting, W. Idler, M. Klenk, E. Lach, G. Laube, K. Wunstel, P. Doussiere, A. Jourdan, F. Pommerau, G. Soulage, L. Goldstein, J.Y. Emery, N. Vodjdani, F. Ratovelomanana, A. Enard, G. Glastre, D. Rondi, R. Blondeau, “Wavelength conversion devices and techniques,” *ECOC '96. 22nd European Conference on Optical Communication*, vol. 4, p 33-40, 1996.
- [16] T. Suhara, M. Fujimura, *Waveguide nonlinear-optic devices*, Springer Verlag, Berlin, 2003.
- [17] M. Asobe, O. Tadanaga, T. Yanagawa, H. Itoh, H. Suzuki, “Reducing photorefractive effect in periodically poled ZnO- and MgO-doped LiNbO<sub>3</sub> wavelength converters,” *Applied Physics Letters*, vol. 78, p 3163, 2001.
- [18] P.A. Franken, A.E. Hill, C.W. Peters, G. Weinreich, “Generation of optical harmonics,” *Phys. Rev. Lett.*, vol. 7, p 118-119, 1961.
- [19] J.F. Pinto, L. Esterowitz, G.H. Rosenblatt, “Tunable UV lasers and their applications,” *Summaries of Papers Presented at the Conference on Lasers and Electro-Optics*, p 139-40, 1995.
- [20] K. Mizuuchi, K. Yamamoto, Y. Kitaoka, M. Kato, “Frequency

- doubling: blue light and UV generation in periodically poled LiTaO<sub>3</sub>/LiNbO<sub>3</sub>,” *IEEE Lasers and Electro-Optics Society 1997 Annual Meeting*, vol. 1, p 110-11, 1997.
- [21] E. Samsøe, P.M. Petersen, S. Andersson-Engels, P.E. Andersen, “Second-harmonic generation of 405-nm light using periodically poled KTiOPO<sub>4</sub> pumped by external-cavity laser diode with double grating feedback,” *Applied Physics B (Lasers and Optics)*, vol. B80, p 861-4, 2005.
- [22] Y. Furukawa, K. Kitamura, S. Takekawa, K. Niwa, H. Hatano, “Stoichiometric Mg:LiNbO<sub>3</sub> as an effective material for nonlinear optics,” *Optics Letters*, vol. 23, p 1892, 1998.
- [23] J. Lee, Y. Mun, S. Do, Y. Ko, D. Kong, B. Choi, J. Kim, C. hong, and D. Jeon, “Laser TV for home theatre,” *Proceedings of the SPIE – The International Society for Optical Engineering*, vol. 4657, p 138, 2002.
- [24] Sung-Nam Lee, J.K. Son, H.S. Paek, Y.J. Sung, K.S. Kim, H.K. Kim, H. Kim, T. Sakong, Y. Park, K.H. Ha, O.H. Nam, “High-power AlInGaN-based violet laser diodes with InGaN optical confinement layers,” *Applied Physics Letters*, vol. 93, p 091109, 2008.
- [25] C.L. Canedy, I. Vurgaftman, W.W. Bewley, C.S. Kim, M. Kim, J.R. Lindle, J.R. Meyer, E.H. Aifer, J.G. Tischler, J.H. Warner, E.M. Jackson, “Recent progress by mid-IR antimonide type-II “W” interband

- cascade lasers and LWIR detectors,” *Proceedings of SPIE*, vol. 6386, p 63860G, 2006.
- [26] M. Troccoli, F. Capasso, R. Colombelli, C. Gmachl, D. Tennant, D.L. Sivco, A.Y. Cho, O.J. Painter, K. Srinivasan, “Mid-IR quantum cascade lasers and amplifiers: recent developments and applications,” The 5th Pacific Rim Conference on Lasers and Electro-Optics, vol. 1, p 10, 2003.
- [27] P.J. McCann, I-Na Chao, H. Sachar, D. McAlister, Chun-Pang Li, Xiao-Ming Fang, Huizhen Wu, K. Namjou, “IV-VI semiconductor growth on silicon substrates and new mid-infrared laser fabrication methods,” *Spectrochimica Acta, Part A*, vol. 55A, p 1999-2005, 1999.
- [28] S. Vasilyev, S. Schiller, A. Nevsky, A. Grisard, D. Faye, E. Lallier, Z. Zhang, A.J. Boyland, J.K. Sahu, M. Ibsen, W.A. Clarkson, “Broadly tunable single-frequency cw mid-infrared source with milliwatt-level output based on difference-frequency generation in orientation-patterned GaAs,” *Optics Letters*, vol. 33, p 1413-1415, 2008.
- [29] O. Tadanaga, Y. Nishida, T. Yanagawa, K. Magari, T. Umeki, M. Asobe, H. Suzuki, “Compact sub-mW mid-infrared DFG laser source using direct-bonded QPM-LN ridge waveguide and laser diodes,” *Proceedings of SPIE*, vol. 6455, p 64550D, 2007.
- [30] O. Tadanaga, T. Yanagawa, Y. Nishida, M. Asobe, H. Suzuki, “Highly efficient mid-infrared difference frequency generation using a

- quasi-phase matched LiNbO<sub>3</sub> ridge waveguide,” *Review of Laser Engineering*, vol. 36, p 64-9, 2008.
- [31] M.M. Fejer, G.A. Magel, D.H. Jundt, R.L. Byer, “Quasi-Phase-Matched Second Harmonic Generation: Tuning and Tolerances,” *IEEE J. Quantum Electron.*, vol. 28, p 2631-2654, 1992.
- [32] T. Suhara, H. Nishihara, “Theoretical analysis of waveguide second harmonic generation phase matched with uniform and chirped gratings,” *IEEE J. Quantum Electron.*, vol. 26, p 1265–1276, 1990.
- [33] P.E. Powers, T.J. Kulp, S.E. Bisson, “Continuous tuning of a continuous wave periodically poled lithium niobate optical parametric oscillatory by use of a fan-out grating design,” *Optical Letters*, vol. 23, p 159, 1998.
- [34] H. Haga, M. Kameoka, S. Yamamoto, “Broadband quasi-phase matched second harmonic generator using taper waveguide,” *Tech. Dig. Nonlinear Optics: Materials, Fundamentals, and Applications Series*, vol. 18, p 367–369, 1992.
- [35] B. Chen, C.Q. Xu, B. Zhou, Y. Nihei, A. Harada, Y. Wang, “Temperature Characteristics of 1.5  $\mu\text{m}$  Band MgO Doped LiNbO<sub>3</sub> Quasi-Phase Matched Wavelength Converters,” *Jpn. J. Appl. Phys.*, vol. 40, p 612-614, 2001.
- [36] Robert W. Boyd, *Nonlinear Optics*, 2<sup>nd</sup> ed, Academic Press, 2002.
- [37] J.A. Armstrong, N. Bloembergen, J. Ducuing, P.S. Pershan,

- “Interactions between light waves in a nonlinear dielectric,” *Phys. Rev.*, vol. 127, p 1918-1939, 1962.
- [38] D.S. Hum, M.M. Fejer, “Quasi-phasematching,” *Comptes Rendus, Physique*, vol. 8, p 180-98, 2007.
- [39] R.L. Byer, “Quasi-phasematched nonlinear interactions and devices,” *Journal of Nonlinear Optical Physics and Materials*, vol. 6, p 549-92, 1997.
- [40] L. Arizmendi, “Photonic applications of lithium niobate crystals,” *Physica Status Solidi C*, vol. 2, p a253-83, 2004.
- [41] K.K. Wong, ed., *Properties of Lithium Niobate*, INSPEC, Inc., 2002.
- [42] [http://en.wikipedia.org/wiki/Lithium\\_niobate](http://en.wikipedia.org/wiki/Lithium_niobate) (accessed Sept. 2008).
- [43] E. Kaldis, ed., “Current topics in materials science,” vol. 1, 1978.
- [44] D.H. Jundt, “Temperature-dependent Sellmeier equation for the index of refraction  $n_e$  in congruent lithium niobate,” *Optics Letters*, vol. 22, p 1553, 1997.
- [45] Brian Jamieson, “Atmospheric gas flow controller for a mass spectrometer used during planetary atmospheric entry,” Final Report, 2004.
- [46] Jean Laconte, Denis Flandre, Jean-Pierre Raskin, “Micromachined Thin-film Sensors for SOI-CMOS Co-integration,” *Birkhäuser*, 2006.
- [47] M.L. Bortz, M.M. Fejer, “Annealed proton-exchanged LiNbO<sub>3</sub> waveguides,” *Optics Letters*, vol. 16, p 1844-6, 1991.

- [48] M.M. Howerton, W.K. Burns, P.R. Skeath, A.S. Greenblatt, "Dependence of refractive index on hydrogen concentration in proton exchanged  $\text{LiNbO}_3$ ," *IEEE Journal of Quantum Electronics*, vol. 27, p 593-601, 1991.
- [49] K. Ito, K. Kawamoto, "Dependence of lattice constant deviation and refractive index on proton concentration in proton-exchanged optical waveguides on a single crystal of  $\text{LiNbO}_3$ ," *Japanese Journal of Applied Physics, Part 1*, vol. 31, p 3882-7, 1992.
- [50] W. Charczenko, I. Januar, A.R. Mickelson, "Modeling of proton-exchanged and annealed channel waveguides and directional couplers," *Journal of Applied Physics*, vol. 73, p 3139, 1993.
- [51] M. Yamada, N. Nada, M. Saitoh, K. Watanabe, "First-order quasi-phased matched  $\text{LiNbO}_3$  waveguide periodically poled by applying an external field for efficient blue second-harmonic generation," *Applied Physics Letters*, vol. 62, p 435-6, 1993.
- [52] M. Fujimura, T. Murayama, T. Suhara, "Quasi-phase-matched difference frequency generation devices with annealed/proton-exchanged  $\text{LiNbO}_3$  waveguides buried by reverse proton exchange," *Japanese Journal of Applied Physics, Part 2*, vol. 43, p L1543-5, 2004.
- [53] Y.N. Korkishko, V.A. Fedorov, S.V. Katin, A.V. Kondrat'ev, "Reverse exchange in the annealed proton exchanged  $\text{LiNbO}_3$  structures for buried waveguides." *7th European Conference on*

*Integrated Optics with Technical Exhibition*, vol. 1, p 395-8, 1995.

[54] A. Ghatak, K. Thyagarajan, *Introduction to Fiber Optics*, Cambridge University Press, 1998.

[55] W.B. Joyce, B.C. DeLoach, "Alignment of Gaussian beams," *Applied Optics*, vol. 23, p 4187-4196, 1984.